Comparison of deterministic and stochastic regime in a model for Cdc42 oscillations in fission yeast

Bin Xu[1], Hye-Won Kang[2], Alexandra Jilkine[1]

1 Department of Applied and Computational Mathematics and Statistics, University of Notre Dame, Notre Dame, Indiana, USA.
2 Department of Mathematics and Statistics, University of Maryland Baltimore County, Baltimore, Maryland, USA.
Keywords: biochemical oscillations, stochastic model, noise-induced phenomena

Abstract

Oscillations occur in a wide variety of essential cellular processes, such as cell cycle progression, circadian clocks and calcium signaling in response to stimuli. It remains unclear how intrinsic stochasticity can influence these oscillatory systems. Here we focus on oscillations of Cdc42 GTPase in fission yeast. We extend our previous deterministic model by Xu and Jilkine to construct a stochastic model, focusing on the fast diffusion case. We use SSA (Gillespie's algorithm) to numerically explore the low copy number regime in this model, and use analytical techniques to study the long-time behavior of the stochastic model and compare it to the equilibria of its deterministic counterpart. Numerical solutions suggest noisy limit cycles exist in the parameter regime in which the deterministic system converges to a stable limit cycle, and quasi-cycles exist in the parameter regime where the deterministic model has a damped oscillation. Near an infinite-period bifurcation point, the deterministic model has a sustained oscillation, while stochastic trajectories start with an oscillatory mode and tend to approach deterministic steady states. In the low copy number regime, metastable transitions from oscillatory to steady behavior occur in the stochastic model. Our work contributes to the understanding of how stochastic chemical kinetics can affect a finite dimensional dynamical system, and destabilize a deterministic steady state leading to oscillations.

1 Introduction

Biological systems have the ability to self-organize at the cellular level. Spatial self-organization can result in spontaneous symmetry breaking of an initially homogeneous distribution to form one or multiple clusters of molecules, as well as dispersal and reformation of these clusters in an oscillatory manner. Assembly and maintenance of active cortical domains in the context of cell growth and division has been termed *cell polarization*. The master regulator of cell polarity in a variety of organisms, from yeast to humans, is the protein Cdc42 [19].

Previous modeling of cell polarization prior to division has focused primarily on budding yeast (*Saccharomyces cerevisae*), specifically on symmetry breaking and establishment of active Cdc42 cortical zones, often via a Turing mechanism [61, 35, 30]. Although there is some evidence that negative feedback may play a role in competition between multiple cortical domains [43], stochastic models of cell polarization have mainly focused on the effects of single or multiple positive feedback loops on the formation of a unique polarity zone [1, 21, 54]. Altschuler and Wu group have shown that in the stochastic regime, mass action positive feedback alone can lead to Cdc42 aggregation [1, 34]. The stochasticity enables the emergence of a spatially heterogeneous state which is very far from the homogeneous equilibrium of

the corresponding deterministic model [34, 50]. Freisinger et al. [21], Hegemann et al. [31] and Lawson et al. [47] have considered effects of multiple positive feedback loops on the robustness of symmetry breaking in response to internal fluctuations and external pheromone gradients. In a recent study on a stochastic version of a Turing-type model of cell polarity [54], Pablo, Ramirez, and Elston suggested that stochasticity can facilitate the speed of Turing-based polarization.

In some circumstances two or more active Cdc42 domains can coexist for some time, and the basis for the switch from a single to multiple polarity zones remains an open question [71]. Here we focus on bipolar cortical zones of Cdc42, as well as spatiotemporal oscillations of Cdc42 from pole to pole that have been observed in fission yeast (*Schizosaccharomyces pombe*) [14]. *S. pombe* cells are rod-shaped and have a constant diameter of 3-4 μm. These cells have a similar aspect ratio and shape as the bacteria *E.coli* but are 100-fold larger in volume. Cell growth occurs at the tip of the cell. Newborn cells grow from the "old" tip (monopolar growth), which have a high level of active Cdc42 (corresponding to an asymmetric steady state of Cdc42) [14]. Oscillations of Cdc42 from pole to pole have been experimentally observed once the cell achieves NETO (new end take-off) and starts bipolar growth from both tips [14]. NETO is a size-dependent transition, occurring once the cell is about 9 μm. NETO can result in either a constant level of Cdc42 at the two tips (symmetric steady state) or out of phase oscillation between the tips [14, 73]. Once the cell reaches approximately 14 μm, it divides by fission, resulting in two daughter cells, each about 7 μm long [12]. Oscillations and fluctuations of Cdc42 may regulate morphology and switch the cell from monopolar to bipolar growth. Several deterministic models for these spatiotemporal oscillations from pole to pole have been proposed, involving both positive and negative feedback loops in Cdc42 regulation [14, 72, 73].

The PDE-ODE model of Cdc42 oscillation in our previous study can be reduced to an ODE system assuming fast diffusion of Cdc42 [73]. We construct a corresponding stochastic model for Cdc42 in the fission yeast and show that the ODE model is a large volume limit of the stochastic model with appropriate scaling. Using Gillespie's Stochastic Simulation Algorithm (SSA) [27], we numerically explore the effect of intrinsic fluctuations on the oscillations in our stochastic model. We are interested in the interplay between stochastic dynamics and nonlinear kinetics. It is known that noise can cause a system that is monostable in the deterministic limit to become bistable in the stochastic model [59]. Other well-known effects of noise added to ODE systems include noise-induced oscillations, termed stochastic resonance [22, 9] and coherence resonance [23, 56]. The former requires a weak periodic external force, while the latter relies on intrinsic noise. Coherence resonance can be found in excitable systems like the FitzHugh-Nagumo model [56] and excitable systems with saddle-node infinite period bifurcations [23], bistable systems like the Duffing-Van der Pol oscillator [75], and systems with Hopf bifurcations [66, 74]. (For mechanism of coherence resonance in excitable and non-excitable systems; see Section 2.4.2 in [25] and references therein.) For an oscillatory dynamical system, it is possible that intrinsic stochasticity can change the creation of a limit cycle with an infinite period which is observed in the deterministic model to a finite period oscillation in the corresponding stochastic model [18].

For our deterministic model of Cdc42 oscillations in fission yeast, we use numerical simulations and power spectrum analysis to answer the following questions:

1. How do stochastic chemical kinetics affect the dynamical behavior when the corresponding deterministic system has multiple stable steady states?

2. How do inherent fluctuations affect the dynamical behavior of the system in the presence or absence of a deterministic limit cycle? Do inherent fluctuations change the dynamical behavior of the system for parameters near the bifurcation point?

3. How do inherent fluctuations affect the period of oscillation?

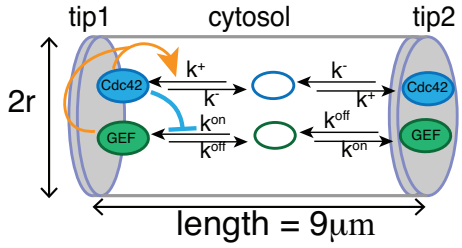

Figure 1: A three-compartmental model for Cdc42 and GEF activation. The left and right (grey) compartments represent two cell tips. The central compartment represents the cytosol. In the stochastic setting, we model a fission yeast cell as a cylinder with a fixed cell length of 9μm. Blue: Cdc42. Green: GEF. Active, membrane-bound Cdc42 and GEF are shown in filled circles. Orange arrow: GEF promotes Cdc42 binding. Blue arrow: Cdc42 inhibits GEF binding. The same reactions take place at tip 2.

2 Models

2.1 Deterministic PDE–ODE model and Reduction to an ODE Model

In our previously published deterministic model [73], the cell is modeled as a one-dimensional domain $[0, L]$ and considers Cdc42 and its regulator GEF in the bulk $(0, L)$ and at two cell poles at $x = 0, L$. At the two poles, there are active membrane-bound Cdc42 molecules with concentrations $c_{1,2}$ and $g_{1,2}$. In the bulk of the cell, there is passive diffusion of inactive Cdc42, $C(x,t)$, and GEF, $G(x,t)$ (see Fig. 1). The full PDE-ODE model is given by

$$\frac{\partial C}{\partial t}(x,t) = D_C \frac{\partial^2 C}{\partial x^2}(x,t), \tag{1a}$$

$$\frac{\partial G}{\partial t}(x,t) = D_G \frac{\partial^2 G}{\partial x^2}(x,t), \tag{1b}$$

$$\frac{\mathrm{d}c_i}{\mathrm{d}t}(t) = k^+(c_i(t), g_i(t))C(L_i,t) - k^- c_i(t), \quad i = 1,2, \tag{1c}$$

$$\frac{\mathrm{d}g_i}{\mathrm{d}t}(t) = k^{\mathrm{on}}(c_i(t))G(L_i,t) - k^{\mathrm{off}} g_i(t), \quad i = 1,2. \tag{1d}$$

Boundary conditions for $C(x,t)$ are taken so that:

$$\mathbf{J}|_{x=0} = -D_C \frac{\partial C}{\partial x}(0,t) = -\frac{\mathrm{d}c_1(t)}{\mathrm{d}t}, \tag{2a}$$

$$\mathbf{J}|_{x=L} = -D_C \frac{\partial C}{\partial x}(L,t) = \frac{\mathrm{d}c_2(t)}{\mathrm{d}t}. \tag{2b}$$

Similarly, boundary conditions for $G(x,t)$ are taken so that:

$$\mathbf{J}|_{x=0} = -D_G \frac{\partial G}{\partial x}(0,t) = -\frac{\mathrm{d}g_1(t)}{\mathrm{d}t}, \tag{3a}$$

$$\mathbf{J}|_{x=L} = -D_G \frac{\partial G}{\partial x}(L,t) = \frac{\mathrm{d}g_2(t)}{\mathrm{d}t}. \tag{3b}$$

We assume that there is mass conservation of Cdc42 and GEF within the cell so that:

$$Ac_1(t) + Ac_2(t) + V\int_0^L C(x,t)\,dx = VC_{tot}, \tag{4}$$

$$Ag_1(t) + Ag_2(t) + V\int_0^L G(x,t)\,dx = VG_{tot}. \tag{5}$$

Here L is a dimensionless length of the cell, V is the volume of the entire cell, while A is the cross-sectional area of cylinder of length L. In dimensional units, $L = 1$ represents a cell length of 9 μm (see Appendix Section A.1 for the units for all parameters in the model). The concentration parameter C_{tot} represents the total concentration in a cell of 9 μm long. In this paper, we fix the cell size L and take C_{tot} as a bifurcation parameter.

The inactive cytosolic (GDP-bound) form of Cdc42 diffuses fast relative to the size of the cell [8]. We assume fast diffusion for both C and G relative to the size of the domain L and obtain the following dimensionless equations (see Appendix Section A.2)

$$C(t) \approx \frac{C_{\text{tot}}L - c_1(t) - c_2(t)}{L}, \quad G(t) \approx \frac{G_{\text{tot}}L - g_1(t) - g_2(t)}{L}. \tag{6}$$

The reduced ODE model for Cdc42 and its GEF at each tip then becomes

$$\frac{\mathrm{d}c_i}{\mathrm{d}t}(t) = k^+(c_i(t), g_i(t))C(t) - k^- c_i(t), \quad i = 1, 2, \tag{7a}$$

$$\frac{\mathrm{d}g_i}{\mathrm{d}t}(t) = k^{\text{on}}(c_i(t))G(t) - k^{\text{off}} g_i(t), \quad i = 1, 2. \tag{7b}$$

Here we focus on the most likely negative feedback implementation discussed in our deterministic model [73]. We assume that active GEF promotes Cdc42 activation while active Cdc42 inhibits the GEF binding. The association rates of Cdc42 and GEF from [73] are nonlinear and given by

$$k^+(c_i, g_i) = (k_0 + k_{cat}c_i^2)g_i, \quad k^{\text{on}}(c_i) = \frac{k^{\text{on}}_{\text{max}}}{1 + \kappa c_i^2}, \tag{8}$$

while dissociation rates with k^- and k^{off} are assumed to be linear. The c_i dependence in the activation rate k^+ represents the recruitment of GEF by Cdc42. For the deterministic model, the nonlinearity c_i^2 is necessary for symmetry breaking in a certain parameter regime. Potential chemical reactions that can lead to this rate have been discussed in [30]. In addition, studies on the biochemistry of Cdc42 binding [17, 69] have reported that the scaffold protein (Scd2) binds to two active Cdc42 molecules, resulting in cooperativity. The polynomial form of the chemical kinetics has been derived and used as an approximation for more complex enzyme kinetics in the glycolytic pathway ([5, 53, 33]). Note that the polynomial form $c_i^2 g_i$ in (8) cannot be interpreted as trimolecular kinetics since it is not physically realistic.

2.2 Stochastic model

2.2.1 Model geometry

For simplicity, we assume diffusion is fast so that we can model the cytosol as a well-mixed cylinder of length L and model each pole (tip) as a small compartment of radius r; see Fig. 1. There are two chemical species (Cdc42 and GEF) in two different forms: (1) active, membrane-bound Cdc42 and GEF; (2) inactive, cytosolic Cdc42 and GEF. We assume that active molecules (filled circles in Fig. 1) only exist at the two end compartments and the inactive forms are found in the cytosol. The transition between inactive and active forms is discussed below.

2.2.2 Binding kinetics

Denote the number of molecules of Cdc42 at tip 1, tip 2, and in the cytosol by $n_1(t), n_2(t)$, and $n_c(t)$, respectively. We represent these numbers using a vector $\vec{X} = (n_1, n_2, n_c)$. Similarly, we express the numbers of GEF using a vector $\vec{Y} = (m_1, m_2, m_c)$. Taking into account binding and unbinding at two poles, we have four possible reactions for X and Y; see below.

(C1) Binding at pole 1: $n_c \xrightarrow{k^+(n_1,m_1)} n_1$;

(C2) Unbinding at pole 1: $n_1 \xrightarrow{k^-} n_c$;

(C3) Binding at pole 2: $n_c \xrightarrow{k^+(n_2,m_2)} n_2$;

(C4) Unbinding at pole 2: $n_2 \xrightarrow{k^-} n_c$.

Here we assume that cytosolic GEF and membrane-bound GEF undergo similar binding kinetics as Cdc42. The binding and unbinding rates for GEF are denoted by k^{on} and k^{off}. The binding rate $k^{\text{on}}(n_1)$ represents the negative regulation of GEF association by active Cdc42. We list the reactions for binding/unbinding below.

(G1) Binding at pole 1: $m_c \xrightarrow{k^{\text{on}}(n_1)} m_1$;

(G2) Unbinding at pole 1: $m_1 \xrightarrow{k^{\text{off}}} m_c$;

(G3) Binding at pole 2: $m_c \xrightarrow{k^{\text{on}}(n_2)} m_2$;

(G4) Unbinding at pole 2: $m_2 \xrightarrow{k^{\text{off}}} m_c$.

It remains to reformulate the binding rate functions k^+ and k^{on} in terms of molecule numbers n_1 and m_1.

2.2.3 Stochastic rates

We need to convert our one-dimensional ODE model to describe a three-dimensional geometry. Specifically, we model the whole cell as a cylinder of length 9μm with radius r; see Fig. 1. We then divide the domain into three compartments with two small end compartments representing the inter-membrane space and one central compartment representing the cytosol. We assume that the length of each end compartment l_ϵ is small and fixed. The volume of the left end compartment is approximated by $V_1 = Al_\epsilon$ and the number of molecules is given by

$$n_1 = 602V_1[c_1] = 602A(l_\epsilon[c_1]).$$

Here $[c_1]$ represents the concentration measured in units of μM. To reduce the number of parameters, we absorb the factor l_ϵ into $[c_1]$ and define a new concentration variable $c_1 = l_\epsilon[c_1]$. It follows that

$$n_1 = 602Ac_1.$$

Similarly, the number of Cdc42 in the cytosol is given by

$$n_c = 602V[C] = 602AL \times 9[C].$$

Here the factor 9 comes from the assumption that the dimensionless parameter $L = 1$ represents a cell of 9μm long. For simplicity, we absorb the factor into $C(t)$ and set $C(t) = 9[C]$; see also Section A.2. This

Reaction	Transition	Deterministic rate	Stochastic rate constant
Cdc42 binding	$n_1 \to n_1 + 1$	$(k_0 + k_{\text{cat}} c_1^2) g_1 (C_{tot} - c_1/L - c_2/L)$	$k_0 \to k_0/(K_a L), k_{cat} \to k_{\text{cat}}/(K_a^3 L)$
Cdc42 unbinding	$n_1 \to n_1 - 1$	$k^- c_1$	k^-
GEF binding	$m_1 \to m_1 + 1$	$k^{\text{on}}_{\text{max}}/(1 + \kappa c_1^2)(G_{tot} - g_1/L - g_2/L)$	$k^{\text{on}}_{\text{max}}/L, \kappa \to \kappa/K_a^2$
GEF unbinding	$m_1 \to m_1 - 1$	$k^{\text{off}} g_1$	k^{off}

Table 1: Reactions in the stochastic model. Only reactions at pole 1 are shown. Replacing n_1 and m_1 by n_2 and m_2 gives the reactions at pole 2. Here the rescaling factor $K_a = 602A$ with $A = \pi r^2$. Cell size: radius $r = 2\mu$m and length $L = 9\mu$m. Parameters used in the deterministic model: $C_{\text{tot}} = 1.5$, $G_{\text{tot}} = 1.5, k^- = 1, k_0 = 0.1, k_{\text{cat}} = 40, k^{\text{on}} = 1, k^{\text{off}} = 0.9 \sim 1, \kappa = 8$. The time scale of 1 unit corresponds to 15 sec.

rescaled concentration represents the cytosolic concentration of Cdc42 in a cell of 9 μm. The number of Cdc42 in the cytosol is given by

$$n_c = 602AL\, C.$$

The conservation equation for the total number of Cdc42 is

$$N_{cdc} = n_1 + n_2 + n_c = 602(c_1 + c_2)A + 602C(t)AL = 602C_{tot}AL. \tag{9}$$

Here C_{tot} represents the total concentration in a cell of length 9μm. It is measured in units of concentration per cross-section area.

Using the relation $n_1 = 602Ac_1$ and $n_c = 602ALC(t)$, we rescale the ODE parameters involved in binding rates as following (See Appendix Section A.3):

$$k_0 \to k_0 \frac{1}{602AL}, \quad k_{\text{cat}} \to k_{\text{cat}} \frac{1}{602AL} \frac{1}{(602A)^2}, \tag{10a}$$

$$\kappa \to \kappa \frac{1}{(602A)^2}, \quad k^{\text{on}}_{\text{max}} \to \frac{k^{\text{on}}_{\text{max}}}{L}. \tag{10b}$$

Denote the area-dependent rescaling parameter by $K_a = 602A$. For a radius $r = 2\mu$m, we have

$$K_a = 602A \approx 7.56 \times 10^3. \tag{11}$$

Then for $C_{\text{tot}} = 1.0$ and $L = 1$, the total number of Cdc42 is given by

$$N_{cdc} = K_a C_{tot} L = 7.56 \times 10^3. \tag{12}$$

The reactions and parameters are listed in Table 1. All the rescaled rates have the same unit as k^-. We use $k^- = 1$ in our stochastic model. This value corresponds to $1/4$ min$=$ 15 sec in physical units as shown in Appendix Section A.3.

3 Results

We begin by simulating the stochastic model using Gillespie's Stochastic Simulation Algorithm [27] and compare differences between stochastic and deterministic variants in the same parameter regime. In particular, we focus on the behavior of the stochastic system close to the parameter regime where the onset of oscillation occurs in the deterministic model.

3.1 Bifurcations in the Deterministic Model

We first consider the bifurcation diagram of the deterministic ODE system (7) in the (C_{tot}, c_1) plane; see Fig. 2(a). Recall that the parameter C_{tot} represents the abundance of Cdc42 and controls the number

of steady states and symmetry breaking. For $C_{\rm tot} \in (0.8662, 1.57)$, there are three stable steady states including a pair of asymmetric steady states (corresponding to most of Cdc42 being at one tip of the cell) and a stable symmetric steady state (corresponding to Cdc42 being evenly divided between two tips). The latter steady state is a focus and we expect to see a damped oscillation near the focus; see Fig. 2(b) for a sample numerical solution. Another key parameter is the GEF dissociation rate $k^{\rm off}$. For a smaller $k^{\rm off} = 0.9$, there is a stable limit cycle for $C_{\rm tot} > 1.09$ that arises via an infinite period bifurcation; see Fig. 2(c). We now fix the total amount of Cdc42 $C_{\rm tot} = 1.1$ and vary $k^{\rm off}$. As $k^{\rm off}$ decreases from 1 to 0.96, there is a Hopf bifurcation at $k^{\rm off} = 0.9774$; see Fig. 2(d). The critical frequency at the Hopf point is $f_{HB} \approx 0.0854$; see the inset in Fig. 2(d). In the next section we show that in the stochastic simulation with the appropriately rescaled parameter values, intrinsic fluctuations can give rise to a quasi-cycle with a dominant frequency close to the frequency $f_{\rm HB}$. For more details of bifurcation analysis of deterministic model please see [73].

3.2 Stochastic Simulations in Absence of Deterministic Limit Cycle

We now consider stochastic simulation results corresponding to the deterministic parameters for $C_{\rm tot} = 1.1, G_{tot} = 1.5$, and $k^{\rm off} = 1.0$ when no limit cycle exists in the deterministic model. The concentrations $C_{\rm tot}$ and $G_{\rm tot}$ are converted the total numbers $(N_{\rm cdc}, N_{\rm gef})$ using equation (9). We consider an arbitrary initial condition

$$n_1 = 0.66 \times N_{\rm cdc}, n_2 = 0.14 \times N_{\rm cdc}, m_1 = 0.1 \times N_{\rm gef}, m_2 = 0.43 \times N_{\rm gef}. \tag{13}$$

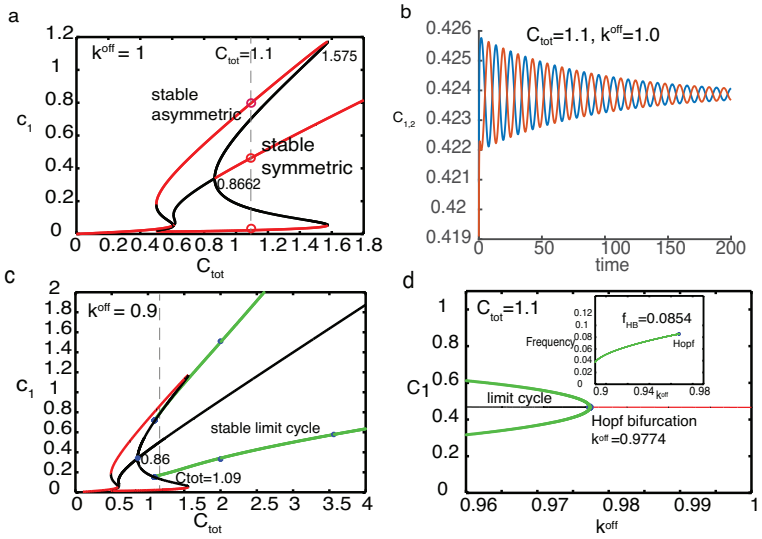

Figure 2: Bifurcation diagrams and sample solution of the ODE model (7). Bifurcation parameters used: $C_{\rm tot}$ and $k^{\rm off}$. (a) Bifurcation diagram of c_1 vs. $C_{\rm tot}$ with $k^{\rm off} = 1$. (b) For a fixed $C_{\rm tot=1.1}$, the symmetric steady state is stable with a pair of complex eigenvalues. The eigenvalue is negative, and the real part of the eigenvalue is small, so the numerical solution shows a sustained damped oscillation. (c) Bifurcation diagram of c_1 vs. $C_{\rm tot}$ with $k^{\rm off} = 0.9$. In contrast to the case when $k^{\rm off} = 1$, the symmetric steady state is now unstable for large L. Instead, we find there is a stable limit cycle for $C_{\rm tot} > 1.09$. This limit cycle persists in the parameter regime while the asymmetric steady state no longer exists. (d) Hopf bifurcation diagrams of the deterministic ODE model with varying $k_{\rm off}$ and a fixed $C_{\rm tot} = 1.1$. As $k^{\rm off}$ changes from 0.96 to 1, a Hopf bifurcation occurs at $k^{\rm off} = 0.9774$. Inset: frequency vs. $k^{\rm off}$. Along the Hopf branch starting at $k^{\rm off} = 0.9774$, the frequency of the limit cycle is small and decreases as $k^{\rm off}$ decreases. Noting also that the frequency is small and thus the period $(T = 1/f)$ is large. As $k^{\rm off}$ further decreased to 0.89 the frequency eventually goes to zero and the period goes to infinity (not shown in the figure). Other parameters: $k_0 = 0.1$, $k_{\rm cat} = 40, n = 2$, $G_{\rm tot} = 1.5$, $L = 1$, $k_m = 1$, $k^{\rm on}_{\rm max} = 1$, $m = 2$, $\kappa = 8$. Red: stable steady states. Black: unstable steady states. Green: stable limit cycles.

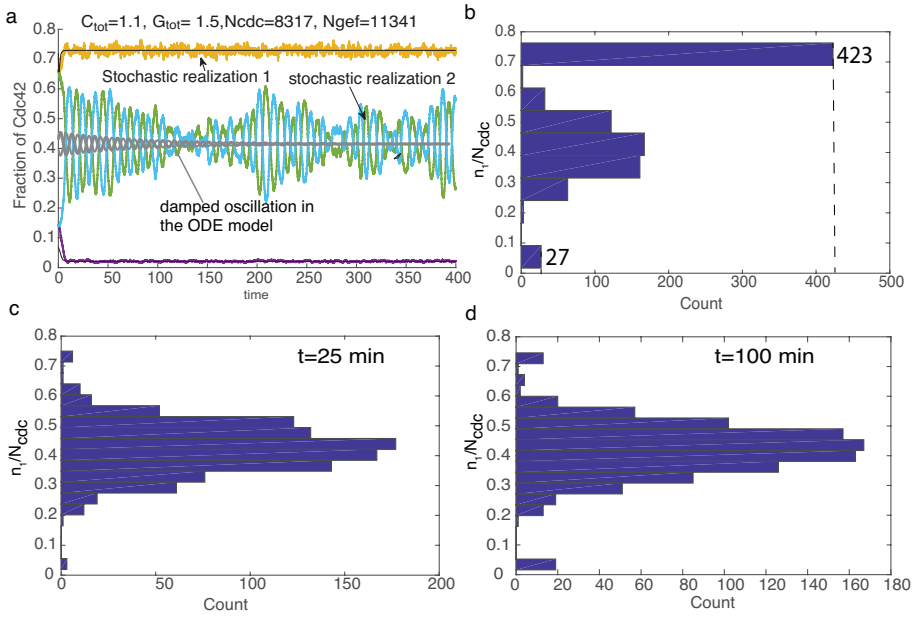

Figure 3: (a) Sample trajectories of Cdc42 (normalized by total number of Cdc42 molecules $N_{\rm cdc}$) at two tips with an asymmetric initial condition $n_1 = 0.66 \times N_{\rm cdc}, n_2 = 0.14 \times N_{\rm cdc}, m_1 = 0.1 \times N_{\rm gef}, m_2 = 0.43 \times N_{\rm gef}$. With the same initial condition, different realizations of stochastic simulations can lead to either an asymmetric steady state (purple and yellow) or an oscillation (blue and green). The time scale of 1 unit corresponds to 15 sec. (b) Histogram of fraction of Cdc42 at tip 1 ($n_1/N_{\rm cdc}$) at time $t = 50 \times 15$ sec. The histogram is computed over 1000 simulations. Among all these 1000 realizations, about half of the trajectories (423/1000) approach the high asymmetric steady state (with $n_1 \approx 0.7 \times N_{\rm cdc}$). The other half of the simulations lead to the oscillations near $n_1 \approx 0.4 \times N_{\rm cdc}$. (c,d) Histogram for stochastic realizations with symmetric initial condition condition: $n_1 = n_2 = 0.42 \times N_{\rm cdc}, m_1 = m_2 = 0.21 \times N_{\rm gef}$.

Two sample stochastic simulations are shown in Fig. 3(a). One sample trajectory (yellow and purple curves) approaches to the asymmetric steady state of the deterministic ODE model, while the other trajectory is oscillatory over time (blue and green). The mean value is close to the symmetric steady state of the deterministic model. To test how frequent each type of trajectory occurs, we plot the histogram of the number of Cdc42 at tip1 at time $t = 50$; see Fig. 3(b). Each scenario occurs with a similar frequency. Specifically, 450 realizations (out of 1000 realizations) approach the asymmetric steady states and about 550 trajectories end up with a y-value (n_1/N_{cdc}) in $[0.3, 0.6]$. This range is consistent with the high and low values of the oscillations shown in the time-course plot (Fig. 3(a)). Note also that the histogram has a small peak where $n_1/N_{cdc} < 0.1$ in Fig. 3(b). This indicates that a part of trajectories (27 trajectories) are close to a lower value of the asymmetric steady states when $t = 50$.

We also considered an initial condition where n_1 and n_2 are symmetric:

$$n_1 = n_2 = 0.42 \times N_{cdc}, m_1 = m_2 = 0.21 \times N_{gef}. \tag{14}$$

The constants 0.42 and 0.21 correspond to the symmetric steady state (c_1, g_1) of the ODE model with $C_{\rm tot} = 1.1$. Again we get an oscillation near the symmetric steady state of the deterministic model. At time $t = 100$ and $t = 400$, most trajectories are oscillatory. A few trajectories approach an asymmetric steady states; see the small peaks near 0 and 0.7; see Fig. 3(c,d).

In summary, we compare the dynamical behavior of the stochastic model and deterministic model in the parameter regime where the deterministic model has a stable symmetric state (focus) and a pair of asymmetric steady states (see Fig. 2a). The main difference is that the stochastic model has a sustained oscillation while the deterministic model has a damped oscillation. In the next section, we explore

the underlying mechanism by analyzing the power spectrum of the time-series generated by stochastic simulations. It turns out the stochastic oscillation has a dominant frequency that is close to the frequency at a Hopf point of the deterministic model.

3.3 Power Spectrum Analysis of Quasi-cycles in Stochastic Model

Recall that our deterministic system has a focus with damped oscillations. As we mention in Section 1, one possible mechanism for noise-induced oscillations is the coherence resonance. Specifically, stochastic kinetics of the dynamical system can destabilize a focus and give rise to a sustained oscillation. These oscillations have a narrow frequency distribution. Power spectrum analysis can be used to find the frequency distribution and to locate the dominant frequency (this refers to the frequency where the distribution has a maximum).

Here we follow the notation and definition of power spectrum density (PSD) in [24]. We first introduce the autocorrelation function of a zero mean process $x(t)$

$$G(\tau) = \lim_{T\to\infty} \frac{1}{T} \int_0^T x(t)x(t+\tau)dt. \tag{15}$$

Here τ is a time lag and the autocorrelation function $G(\tau)$ measures the influence of a value at time t on the value at time $t+\tau$. As stated in [24], the power spectrum density $S(\omega)$ is related to Fourier transform of the autocorrelation function

$$S(\omega) = \lim_{T\to\infty} \frac{1}{2\pi T} \left| \int_0^T \mathrm{e}^{-i\omega t} x(t)dt \right|^2 = \frac{1}{2\pi} \int_{-\infty}^{\infty} \mathrm{e}^{-i\omega\tau} G(\tau)d\tau. \tag{16}$$

For an ergodic process, we have $G(\tau) = \langle x(t)x(t+\tau)\rangle$ where $\langle\cdot\rangle$ denotes the ensemble average. Let $\tilde{x}(\omega)$ denote the Fourier transform of $x(t)$, then the covariance of the Fourier coefficient satisfies

$$\langle \tilde{x}(\omega)\tilde{x}(\omega')\rangle = \delta(\omega+\omega')S(\omega). \tag{17}$$

We now define the power spectrum density for the chemical species in our Cdc42-GEF system. As an example, we consider Cdc42 at tip 1 (n_1) and define its power spectrum density ($S_1(\omega)$) by

$$S_1(\omega) = \frac{1}{2\pi} \int_{-\infty}^{\infty} \mathrm{e}^{-i\omega\tau} G(\tau)d\tau = \frac{1}{2\pi} \int_{-\infty}^{\infty} \mathrm{e}^{-i\omega\tau} \left\langle (n_1(t) - n_1^{ss})(n_1(t+\tau) - n_1^{ss}) \right\rangle d\tau. \tag{18}$$

Here n_1^{ss} denotes the steady-state number of Cdc42 at tip 1. Note that the definition in equation (18) represents the two-sided power spectrum density. Multiplying the expression in (18) by 2 gives the one-sided power spectrum density (this is used in [64]). In general, it is difficult to calculate the PSD using the definition since a closed-form expression for the solution $n_1(t)$ is unknown. Alternatively, McKane et al. [51] has developed an analytic approximation for the power spectrum. Their method is based on a Langevin equation for the chemical reactions using the linear noise approximation. Fourier transform is then applied to the Langevin equation to derive a theoretical approximation for the power spectrum density. See also section 2 of [63] for a detailed discussion of the method.

3.3.1 Power spectrum estimation using the linear noise approximation

Here we use the method developed by McKane et al. [51] to estimate the power spectrum of inherent fluctuations in our stochastic model near the deterministic steady state. Recall that there are six chemical species in our three-compartmental model and two conservation equations. Following the analysis in the

cyclic Lotka–Volterra model [58], we reduce the number of chemical species to four using the conservation equation of the total number of Cdc42 (GEF). Introduce the concentration variable

$$\mathbf{u} = (c_1, c_2, g_1, g_2). \tag{19}$$

In this section, we use both u_i, $i = 1, 2, 3, 4$, and c_1, c_2, g_1, g_2 to refer the component of $\mathbf{u}$. To find the power spectral density, it is more convenient to rewrite the deterministic ODE for species i in the generic form

$$\frac{\mathrm{d}u_i}{\mathrm{d}t} = \sum_{r=1}^{p} S_{ir} f_r(\mathbf{u}).$$

Here S is the stoichiometric matrix and S_{ir} refers to its (i, r)th component, r labels the single-step reaction, f_r is the reaction rate, and p is the number of single-step reactions. For our Cdc42-GEF system, the total number of reactions p equals to 8. In addition, we set the first four reactions to be the activation of Cdc42 at pole 1, deactivation of Cdc42 at pole 1, activation of Cdc42 at pole 2, and deactivation of Cdc42 at pole 2. The other four reactions represent the GEF binding kinetics in the same order. The expressions of the reaction rates $f_i (1 \le i \le 8)$ are given below.

$$f_1 = (k_0 + k_{\mathrm{cat}} c_1^2) g_1 (C_{tot} - c_1/L - c_2/L), \quad f_2 = k^- c_1, \tag{20a}$$

$$f_3 = (k_0 + k_{\mathrm{cat}} c_2^2) g_2 (C_{tot} - c_1/L - c_2/L), \quad f_4 = k^- c_2, \tag{20b}$$

$$f_5 = \frac{k_{\max}^{\mathrm{on}}}{1 + \kappa c_1^2} (G_{tot} - g_1/L - g_2/L), \quad f_6 = k^{\mathrm{off}} g_1, \tag{20c}$$

$$f_7 = \frac{k_{\max}^{\mathrm{on}}}{1 + \kappa c_2^2} (G_{tot} - g_1/L - g_2/L), \quad f_8 = k^{\mathrm{off}} g_2. \tag{20d}$$

In the following calculation, we take $L = 1$. The corresponding stoichiometric matrix S is a 4 by 8 matrix and is given by

$$S = \begin{pmatrix} S_1 & 0 \\ 0 & S_1 \end{pmatrix}, \quad S_1 = \begin{pmatrix} 1 & -1 & 0 & 0 \\ 0 & 0 & 1 & -1 \end{pmatrix}. \tag{21}$$

We now quantify the effect of inherent fluctuations near a steady state $\mathbf{u}^* = (c_1^*, c_2^*, g_1^*, g_2^*)$. Let N be the system size and we take $N = 602A$. We denote a vector for species copy numbers after a time change as $\mathbf{n}(\beta t) = (n_1(\beta t), n_2(\beta t), m_1(\beta t), m_2(\beta t))$ and the scaled difference from the deterministic steady state as $\boldsymbol{\xi} = (\xi_1, \xi_2, \xi_3, \xi_4)$. Then, we define the scaled difference as

$$\xi_j(t) = \sqrt{N} \left(\frac{n_j(\beta t)}{N} - u_j^* \right) \quad j = 1, \cdots, 4. \tag{22}$$

The fluctuations ξ_j around the steady state u_j^* satisfies the Langevin equation (the derivation uses a system-size expansion [67])

$$\frac{\mathrm{d}\xi_j}{\mathrm{d}t}(t) = \sum_{j'=1}^{4} A_{jj'} \xi_{j'}(t) + \eta_j(t) \tag{23}$$

with white noise terms satisfying

$$E[\eta_j(t)] = 0, \quad E[\eta_j(t) \eta_{j'}(t')] = D_{jj'} \delta(t - t') \tag{24}$$

where δ is a Dirac delta function. The matrix A is the Jacobian at the fixed point $\mathbf{u}^*$ and its jth column is given by

$$A_{1j} = \left. \frac{\partial (f_1(\mathbf{u}) - f_2(\mathbf{u}))}{\partial u_j} \right|_{\mathbf{u}=\mathbf{u}^*}, \qquad A_{2j} = \left. \frac{\partial (f_3(\mathbf{u}) - f_4(\mathbf{u}))}{\partial u_j} \right|_{\mathbf{u}=\mathbf{u}^*},$$

$$A_{3j} = \left. \frac{\partial (f_5(\mathbf{u}) - f_6(\mathbf{u}))}{\partial u_j} \right|_{\mathbf{u}=\mathbf{u}^*}, \qquad A_{4j} = \left. \frac{\partial (f_7(\mathbf{u}) - f_8(\mathbf{u}))}{\partial u_j} \right|_{\mathbf{u}=\mathbf{u}^*}.$$

A direct matrix calculation gives

$$D = \text{diag}(f_1 + f_2, f_3 + f_4, f_5 + f_6, f_7 + f_8) \tag{25}$$

where $\text{diag}(d_1, \cdots, d_n)$ represents an $n \times n$ diagonal matrix with the ith element as d_i.

Next, we proceed to calculate the power spectrum by taking the Fourier transform of the Langevin equation (23). Denote the Fourier transform of $\xi_j(t)$ by

$$\tilde{\xi}_j(\omega) = \frac{1}{2\pi} \int_{-\infty}^{\infty} \mathrm{e}^{-i\omega t} \xi_j(t) dt,$$

and define vectors $\tilde{\boldsymbol{\xi}} = \left(\tilde{\xi}_1, \tilde{\xi}_2, \tilde{\xi}_3, \tilde{\xi}_4\right)$ and $\tilde{\boldsymbol{\eta}} = (\tilde{\eta}_1, \tilde{\eta}_2, \tilde{\eta}_3, \tilde{\eta}_4)$. Taking the Fourier transform of equation (23) gives

$$i\omega \tilde{\xi}_j(\omega) = \sum_{j'} A_{jj'} \tilde{\xi}_j(\omega) + \tilde{\eta}_j(\omega). \tag{26}$$

which can be written as, $\Phi(\omega)\tilde{\boldsymbol{\xi}}(\omega) = \tilde{\boldsymbol{\eta}}(\omega)$ where Φ is a 4×4 matrix with each element defined as $\Phi_{jj'} = -A_{jj'} + i\omega\delta_{jj'}$. Solving the linear system $\Phi(\omega)\tilde{\boldsymbol{\xi}}(\omega) = \tilde{\boldsymbol{\eta}}(\omega)$ for $\tilde{\boldsymbol{\xi}}(\omega)$ gives

$$\tilde{\boldsymbol{\xi}}(\omega) = \Phi^{-1}(\omega)\tilde{\boldsymbol{\eta}}(\omega) \tag{27}$$

where where Φ^{-1} is an inverse of Φ. Note that the Fourier transform of the white-noise term $\eta_j(t)$ satisfies

$$\langle \tilde{\eta}_j(\omega) \rangle = 0, \quad \langle \tilde{\eta}_j(\omega) \tilde{\eta}_{j'}(\omega') \rangle = D_{jj'} \delta(\omega + \omega'). \tag{28}$$

It follows that

$$\begin{aligned} \left\langle \tilde{\boldsymbol{\xi}}(\omega) \tilde{\boldsymbol{\xi}}(\omega')^T \right\rangle &= \left\langle \Phi^{-1}(\omega) \tilde{\boldsymbol{\eta}}(\omega) \tilde{\boldsymbol{\eta}}(\omega')^T \Phi^{-1}(\omega')^T \right\rangle \\ &= \delta(\omega + \omega') \Phi^{-1}(\omega) D \Phi^{-1}(\omega')^T \\ &= \delta(\omega + \omega') \Phi^{-1}(\omega) D \left(\Phi^*(-\omega')\right)^{-1} \end{aligned} \tag{29}$$

where Φ^* represent the conjugate transpose of Φ. Setting $\omega' = -\omega$ in equation (29), then

$$\left\langle |\tilde{\xi}_j(\omega)|^2 \right\rangle = \left\langle \left(\tilde{\boldsymbol{\xi}}(\omega) \tilde{\boldsymbol{\xi}}(-\omega)^T \right)_{jj} \right\rangle = \delta(0) \left(\Phi^{-1}(\omega) D \left(\Phi^*(\omega)\right)^{-1} \right)_{jj}.$$

Using equation (17), we obtain the power spectrum of the fluctuation ξ_j

$$S_j(\omega) = \left(\Phi^{-1}(\omega) D \left(\Phi^*(\omega)\right)^{-1} \right)_{jj}. \tag{30}$$

A closed form expression for $S_j(\omega)$ is complicated due to the calculation of the inverse matrix Φ^{-1}. Here we compute $S_j(\omega)$ numerically for an arbitrary ω and then plot $S_j(\omega)$ as a function of ω. For the parameters $C_{\text{tot}} = 1.1$ and $C_{\text{tot}} = 1.6$, the power spectrum density is shown by the red curve in Fig. 4(a,c). As expected, the power spectrum has a maximum at a dominant frequency $\omega_c \approx 0.54$. Note that ω refers to the angular frequency, the regular frequency f (cycles per unit time) is given by $f = \omega_c/(2\pi) = 0.0861$, which is close the frequency at the Hopf bifurcation point $f = 0.0854$; see the inset of Fig. 2(d). The averaged frequency obtained using 2000 stochastic realizations is also close to the Hopf frequency; see the histogram Fig. 4(b). Similar results are observed for a large $C_{\text{tot}} = 1.6$ (in this case, the deterministic model is uni-stable). We now compare the theoretical approximation (equation (30)) with the stochastic simulation. Both results predict a similar dominant frequency. One major difference lies in the width of

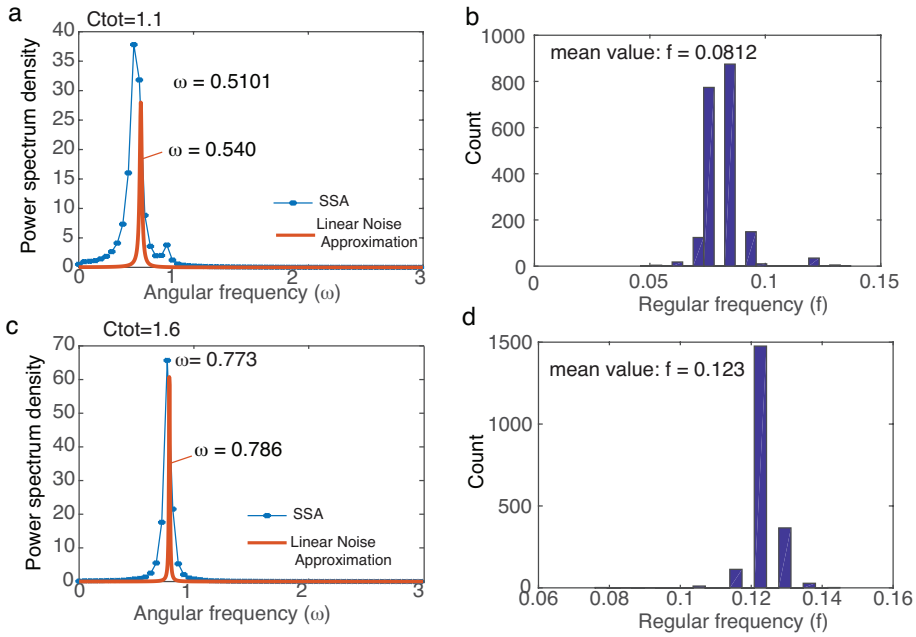

Figure 4: (a) Power spectrum density of the number of Cdc42 at tip1 with $C_{\text{tot}} = 1.1$. Red: theoretical approximation of power spectrum density $S_1(\omega)/N$ (normalized by the integral of $S_1(\omega)/N$). Blue: averaged numerical power spectrum density calculated using 2000 realizations. For each realization, we compute the power spectrum density using a fast Fourier transform; see Section B.2 for details. The numerical power spectrum density is normalized by the total power (integral of $S(\omega)/(2\pi)$) computed using the trapezoidal rule. (b) Histogram of dominant frequencies (f) of 2000 realizations. The mean regular frequency is obtained as $f \approx 0.0812$, which is close to the frequency at the Hopf bifurcation point $f_{\text{HB}} \approx 0.085$; see Fig. 2(d). (c,d) Same plots for $C_{\text{tot}} = 1.6$.

the band near the dominant frequency. In comparison to the stochastic simulation, the power spectrum approximation using a linear noise approximation has a smaller frequency window near the dominant frequency. Also, for the case with $C_{\text{tot}} = 1.1$, the power spectrum density of the stochastic simulation data has another small peak between 0.5 and 1. This additional peak is not captured by the linear noise approximation.

Another way to detect the dominant frequency is to consider the determinant $|\det \Phi(\omega)|$ [15, 64]. Note that the expression $S_1(\omega) = \Phi^{-1}(\omega) D \left(\Phi^*(\omega)\right)^{-1}$ is singular when the determinant $\det \Phi(\omega)$ is zero. Recall that $\Phi(\omega) = A - i\omega I_4$ where A is the Jocobian matrix at the steady state. Near a Hopf bifurcation point of the deterministic model, the Jacobian A has a pair of conjugate eigenvalues $\lambda_{1,2} = \gamma \pm i\omega_0$ with the real part γ close to zero. It follows that the matrix Φ has a pair of conjugate eigenvalues which are given by $\lambda_{1,2} - i\omega = \gamma \pm i(\omega_0 - \omega)$. As ω approaches ω_0 (i.e., $\omega = (1-\epsilon)\omega_0$ with $|\epsilon| \ll 1$), the magnitude of the eigenvalue $|\lambda_{1,2} - i\omega|^2 = \gamma^2 + \epsilon^2\omega_0^2$ becomes small. As a result, $\det |\Phi^{-1}(\omega)|$ is large near the Hopf frequency ω_0.

3.4 Stochastic Simulations in the Presence of a Deterministic Limit Cycle

We now focus on the parameter regime where the deterministic ODE model has a limit cycle. The bifurcation diagram of the deterministic model is shown in Fig. 2(c). We briefly summarize the bifurcation diagram, which is described in more detail in [73]. An infinite period bifurcation occurs at $C_{\text{tot}} \approx 1.09$. For $C_{\text{tot}} > 1.09$, there is a stable limit cycle. For an intermediate $C_{\text{tot}} \in (1.09, 1.558)$, the deterministic system is tristable with a pair of stable asymmetric steady states and a stable limit cycle. For $C_{\text{tot}} > 1.558$,

the steady states vanish and only the limit cycle persists. For C_{tot} near the bifurcation point $C_{\text{tot}} \approx 1.09$, we show the numerical solutions in Fig. 5(a-c).

Note that in a stochastic setting, there is an additional parameter $N = 602A$ which represents the the system size. Over a finite time interval, the stochastic model with appropriate scaling approaches the deterministic model as the system size gets large ($N \to \infty$) (see Appendix Section A.4) [44, 45]. However, if a deterministic model has multiple steady states, its stochastic counterpart may have a different steady-state behavior as $t \to \infty$. For example, a stochastic model may approach a steady state which is unstable in the deterministic model; see Keizer's paradox [39]. Mathematically speaking, the exchange of two limits ($t \to \infty$ and $N \to \infty$) can be problematic; see [68] for an explanation of Keizer's paradox. More recent work identified a general class of stochastic chemical reaction networks where the systems always exhibit extinction events under some conditions while a subset of chemical species maintains robust steady-state concentrations in the corresponding deterministic mass-action systems regardless of the total concentration levels of the systems [4]. The work was extended to find sufficient conditions for extinction events under the stochastic setting [36]. Though this class of stochastic chemical reaction networks shows extinction events, it was analytically proven that the long-term behavior before the extinction event of the stochastic model agrees with the limiting behavior of the deterministic system [16, 3]. Here we focus on the dynamics during a finite time and perform stochastic simulation to explore how the system behavior changes as the system size N, the concentration parameter C_{tot}, and the GEF dissociation rate k_{off} change.

In the following, we consider the parameter regime where the deterministic model has a stable limit cycle but no stable steady states and the parameter regime where multiple stable steady states and a stable limit cycle coexist. For the former, the stochastic model also has stochastic oscillations and stochastic oscillation persists as the copy number is reduced to hundreds. The averaged period of stochastic oscillations is consistent with the period of the deterministic oscillation. On the other hand, in the parameter regime where the deterministic model has multiple attractors, we observe stochastic transitions when the copy number is in hundreds. Finally, we explore the sensitivity of the deterministic system to initial perturbations near a bifurcation point.

3.4.1 Stochastic oscillation and transition to steady behavior

How does intrinsic stochasticity affect the limit cycle of the equivalent ODE system? What happens when a limit cycle coexists with stable steady state(s)? Consider the symmetric initial condition:

$$n_1 = n_2 = 0.42 \times N_{\text{cdc}}, \quad m_1 = m_2 = 0.21 \times N_{\text{gef}}.$$

Recall that N_{cdc} and N_{gef} are determined by

$$N_{\text{cdc}} = 602AC_{\text{tot}} = 602\pi r^2 C_{\text{tot}}, \quad N_{\text{gef}} = 602AG_{\text{tot}} = 602\pi r^2 G_{\text{tot}}.$$

We can change the total number N_{cdc} by either changing the concentration parameter C_{tot} or the system-size $N = 602\pi r^2$. For simplicity, we fix the GEF concentration parameter $G_{\text{tot}} = 1.5$. If we change the system size, then the number of Cdc42 (N_{cdc}) and the number of GEF (N_{gef}) change simultaneously where the ratio $N_{\text{cdc}}/N_{\text{gef}} = C_{\text{tot}}/G_{\text{tot}}$ stays fixed. In the following, we show stochastic simulation results for different C_{tot} and N. We change the system size N by changing the radius of the cell, r, since it does not appear in the deterministic ODE model, and does not change the length of the cell. Furthermore, in fission yeast, the cell curvature (which is affected by the radius) is known to influence the size of the active Cdc42 zone [10]. The default value for r is taken to be 2 μm. For $r = 2$ μm and $C_{\text{tot}} = 1.0$, the corresponding number of Cdc42 is $N_{cdc} = 7565$.

We fix $C_{\text{tot}} = 1.1$ and vary r as well as the initial molecular copy numbers correspondingly in the stochastic model as shown in Fig. 5(d-f). For $r = 1, 2$, and 4 μm, sample trajectories start with an oscillatory mode and then transit to an asymmetric steady state. Note that this behaviour is different

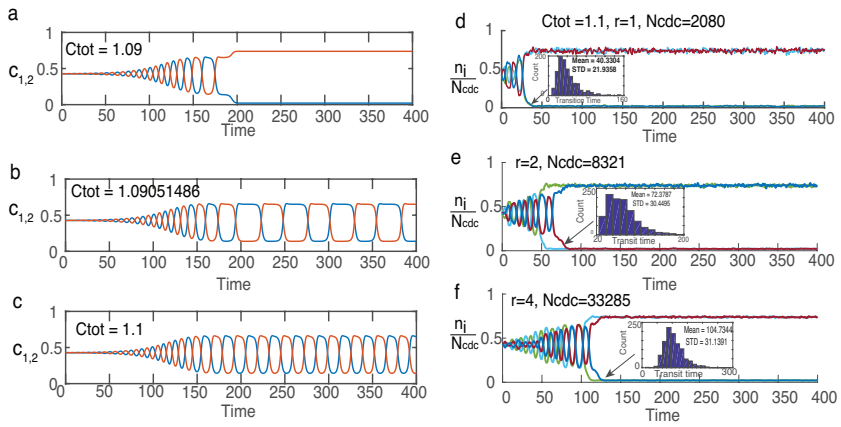

Figure 5: Deterministic and stochastic trajectories near $C_{\text{tot}} = 1.1$. (a-c) Numerical solution of the deterministic model with $C_{\text{tot}} = 1.09, 1.09051486$, and 1.1. (d-f) Time-course plots of two stochastic realizations with $C_{\text{tot}} = 1.1$ and different system sizes. Here we change the system size $N = 602\pi r^2$ by changing the cell radius r. For $r = 1, 2$, and 4 μm, the stochastic solution oscillates and then switch to an asymmetric steady state. The behavior for the stochastic model with $C_{\text{tot}} = 1.1$ is similar to the behavior of the deterministic model with a smaller $C_{\text{tot}} = 1.09$; see Fig. 5(a). Increasing the system size may delay the transition to an asymmetric steady state; see histograms of transition times in Fig. 5(d-f). The initial condition is given by equation (14).

from the deterministic model at $C_{\text{tot}} = 1.1$ since the deterministic model has a sustained oscillation. Similar results are obtained with an even larger system size $r = 15$ (not shown). However, the behavior of the stochastic trajectory (Fig. 5(d-f)) is similar to the behavior of the deterministic model at a smaller $C_{\text{tot}} = 1.09$ (Fig. 5(a)), which is close to the bifurcation point. Hence, based on numerical simulation we hypohesize that increasing the system-size does not give rise to sustained oscillation but may lead to a delay in the transition time to an asymmetric steady state; see histograms of transition times in Fig. 5(d-f). To detect if oscillations occur in different stochastic realizations, we repeat the stochastic simulations for 1000 times and plot the histogram of the number of Cdc42 at tip 1 (normalized by N_{cdc}) at a large time $t = 400$; see Fig. 6(a). The resulting histogram has two peaks located at the asymmetric steady states. The numerics suggest that in the stochastic model trajectories approach an asymmetric steady state and oscillations are unlikely to occur for $C_{\text{tot}} = 1.1$ (see section 3.4.3).

We then choose a high value $C_{\text{tot}} = 1.6$ where the deterministic ODE model has a stable limit cycle (no stable steady states exist). In Fig. 7(a), we show sample stochastic trajectories for $r = 2, 1$, and 0.5 μm. Oscillations persist in the stochastic variant in all these three cases. A histogram of the number of Cdc42 at tip 1 with $C_{\text{tot}} = 1.6$ and $r = 1$ μm is shown in Fig. 6(f). As the system size parameter r decreases to 0.5, the total number of Cdc42 is reduced to 756. With such a low copy number, oscillations still exist although some irregular behavior in the periodicity emerges; see the bottom curve in Fig. 7(a).

Finally, we consider two cases with intermediate values $C_{\text{tot}} = 1.4$ and $C_{\text{tot}} = 1.3$. For these two values, the deterministic model has a pair of stable asymmetric steady states and a stable limit cycle. In the stochastic model, coexistence of these three possibilities is observed when $C_{\text{tot}} = 1.3$ and $r = 2$; see Fig. 7(c) (time-course plot) and Fig. 6(b) (histogram). As C_{tot} is increased to 1.4, oscillations are more likely to occur; see Fig. 7(b) and Fig. 6(c). Now let us consider the effect of reducing the system size for $C_{\text{tot}} = 1.3, 1.4$. In both cases, as the system-size parameter r changes from 2 to 1, trajectories are more likely to approach an asymmetric steady state; see the middle panels in Fig. 7(b,c) and histograms in Fig. 6(d,e). For a much smaller $r = 0.5$, there are random transitions between two asymmetric steady states; see the bottom panels in Fig. 7(b,c). For $r = 0.5$, robust oscillations are observed only when $C_{tot} > 1.6$ ($N_{cdc} > 756$).

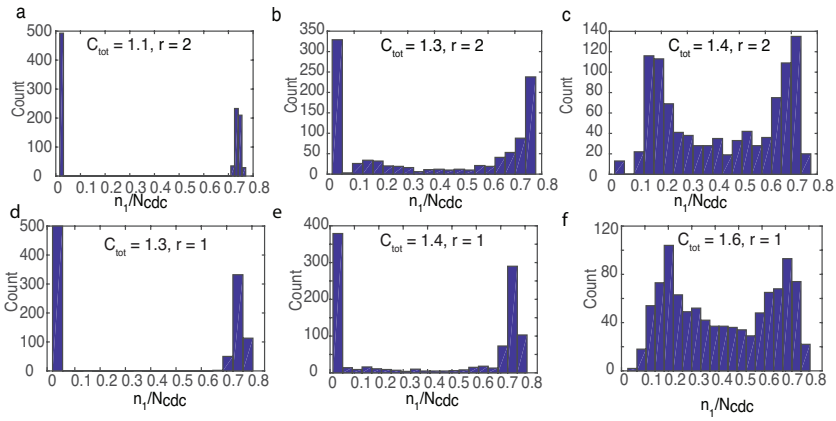

Figure 6: Histograms of the number of Cdc42 molecules at tip 1(normalized by N_{cdc}) at time $t = 400$ for different $C_{\rm tot}$. (a) $C_{tot} = 1.1$ and $r = 2$ μm. All 1000 trajectories approach an asymmetric steady state of the deterministic model. With a symmetric initial condition, it is equally likely for a trajectory (n_1/N_{cdc}) to approach an asymmetric steady state with a high value ($c_1 > c_2$) or a low value ($c_1 < c_2$); see red curves in Fig. 2(c). Oscillations are not observed in stochastic realizations. (b) $C_{tot} = 1.3$ and $r = 2$. Oscillations and two asymmetric steady states coexist. About 1/3 of the trajectories are near the low asymmetric steady state and another 1/3 trajectories are near the high asymmetric steady state. The rest of the trajectories have end-points distributed between the two steady states. (c) $C_{tot} = 1.4, r = 2$. Most of the trajectories are oscillatory. Note that the peak near the low asymmetric steady state is small. (d,e,f) $r = 1$ and $C_{\rm tot} = 1.3, 1.4, 1.6$, respectively. Oscillations disappear for a small $C_{\rm tot} = 1.3$ when r is reduced to 1. Number of bins used in histogram: 20. Number of stochastic realizations: 1000.

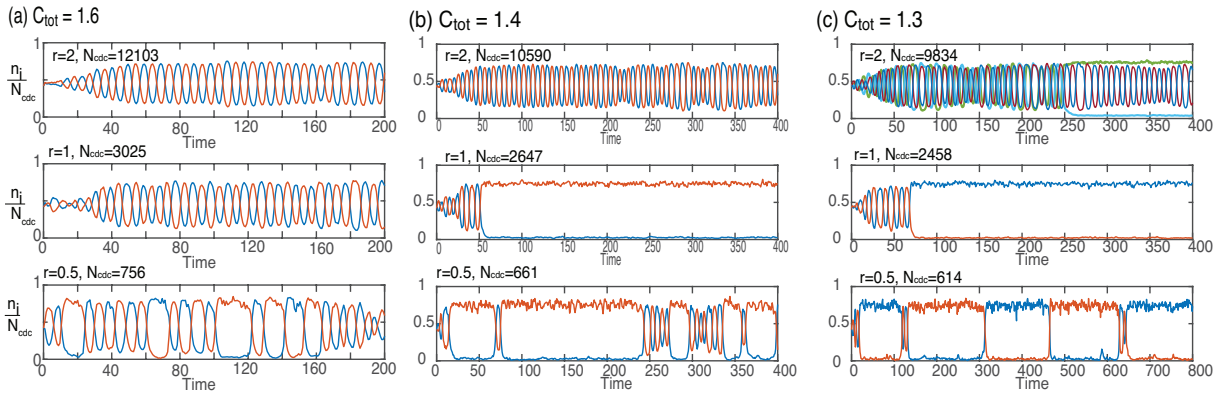

Figure 7: Sample stochastic trajectories for $C_{\rm tot} = 1.6, 1.4, 1.3$ and different values of system size parameter r. In each panel, we show one stochastic realization for $r = 2, 1$, and 0.5. (a) $C_{\rm tot} = 1.6$. For a default value $r = 2$ and $N = O(10^5)$, we observe a regular anti-phase oscillation. As r decreases to 0.5, the period of oscillation becomes irregular. (b) $C_{\rm tot} = 1.4$. Note that this value lies in the multi-stability region of the deterministic ODE where a pair of stable asymmetric steady states and a stable limit cycle coexist; see Fig. 2(c). Depending on the system-size, the stochastic system at time $t = 400$ may have a "favored" state (oscillation for $r = 2$ and asymmetric state for $r = 1$). When $r = 0.5$, the number of Cdc42 is small ($O(10^2)$). The stochastic trajectory has an irregular behavior with transitions between an oscillatory mode and an asymmetric state. (c) $C_{\rm tot} = 1.3$. For $r = 2$, two arbitrary stochastic realizations show that stochastic oscillations and asymmetric steady state can co-exist. For $r = 1$, the behavior is similar to the case when $C_{\rm tot} = 1.4$. For $r = 0.5$, there is a transition between two asymmetric steady states. Oscillations occur less frequently. The initial condition is given in equation (14). The time scale of 1 unit corresponds to 15 sec.

3.4.2 Period of oscillation

We now compare oscillations in deterministic and stochastic models. For simplicity, we focus on the parameter regime where the deterministic system converges to a stable limit cycle and there are no stable steady states, so we do not have to consider metastable switching from a limit cycle to a steady state and back. Stochastic simulations show that a noisy limit cycle exists in this regime and we compute the averaged period of 1000 stochastic cycles and compare with the period of deterministic limit cycle, which we computed using XPPAUT. For the deterministic solution, we use the initial condition $(c_1, c_2, g_1, g_2) = (0.42, 0.42, 0.21, 0.21) + \epsilon(1, -1, 1, 1)$ with $\epsilon = 0.001$. This corresponds to the symmetric branch of the bifurcation diagram Fig. 2(c). The small perturbation is included so that the deterministic system converges to an oscillatory solution. Such an initial perturbation is not necessary for a stochastic model. The inherent fluctuations coming from the discreteness of molecular numbers and the random nature of reactions are sufficient to destabilize a symmetric state and to converge to an oscillation.

In Fig. 8(a), we plot the period of oscillation as a function of the concentration parameter C_{tot} for $r = 2$ μm. In both stochastic and deterministic models, the period decreases as the amount of Cdc42 C_{tot} increases. We then fix $C_{\text{tot}} = 1.6$ and vary the parameter k^{off} (GEF dissociation rate). For the deterministic model, a Hopf bifurcation occurs at $k^{\text{off}} = 0.9903$ and a stable limit cycle exists for $k^{\text{off}} < 0.9903$. Above the bifurcation point, the deterministic model has a stable steady state while the stochastic model has a quasi-cycle. Here we focus on the regime $k^{\text{off}} < 0.99$ where stochastic and deterministic limit cycles exist. In Fig. 8(b), we plot the period of deterministic oscillation (green) and the averaged period of stochastic oscillation (blue) as a function of k^{off}. The results in both models are consistent. Note that the period increases quickly from 10 to 43 (in dimensionless units) as the parameter k^{off} decreases from 0.9 to 0.7. This fast change in period can be reduced if we reduce the autocatalysis rate (e.g., $k_{cat} = 20$ instead of $k_{cat} = 40$); see inset in Fig. 8(b). It then stays near 43 for a wide range of $k^{\text{off}} \in (0.3, 0.7)$. In this parameter regime, we observe relaxation oscillations in both stochastic and deterministic models; see Fig. 8(c,d) for solutions with $k^{\text{off}} = 0.7$. The model, thus predicts that by varying the residence time of active GEF on the cell tips, $1/k^{\text{off}}$, one should observe a change in period of the oscillation even if the amount of Cdc42 and GEF in the cell does not change.

3.4.3 Sensitivity to perturbations near a bifurcation point

Finally, we explore the dynamics near the infinite period bifurcation point $C_{\text{tot}} \approx 1.1$. Under small perturbation of the initial condition, the deterministic model can converge to different attractors. One initial condition that can lead to an oscillation is given by

$$[c_1(0), c_2(0), g_1(0), g_2(0)] = [0.8980, 0.1809, 0.0770, 0.4300]. \tag{31}$$

This initial condition has two main features: (1) the active Cdc42 is high at tip 1($c_1 > c_2$), while the GEF at the same tip is low ($g_1 \ll g_2$); (2) the inactive Cdc42 (substrate) $C_{\text{tot}} - c_1 - c_2 \approx 0.0211$ is almost zero while the GEF is still plentiful. Therefore, the binding rate of Cdc42 at tip1 is low and its concentration decreases quickly. As a result, more free Cdc42 becomes available and the Cdc42 concentration at tip 2 increases quickly due to the strong positive feedback. The accumulation at tip 2 triggers the negative feedback and inhibits GEF binding. As a result, g_2 decreases which leads to a decrease in Cdc42 binding rate, resulting in an oscillation. See Fig. 9(a,b) for the time-course plot and Fig. 9(c,d) for the limit cycle visualized in the phase plane. Next, we illustrate how the deterministic system can be perturbed away from the limit cycle. Consider two small perturbations of the initial condition (31):

$$[c_1(0), c_2(0), g_1(0), g_2(0)] = [0.8980, 0.1809, 0.0770, 0.4300] + [0, 0, 0, 0.01]. \tag{32}$$

$$[c_1(0), c_2(0), g_1(0), g_2(0)] = [0.8980, 0.1809, 0.0770, 0.4300] + [0, -0.0209, 0, 0]. \tag{33}$$

As we increase the initial amount of GEF at tip 2 by 0.01 (IC (32)), the system approaches a steady state with $c_2 > c_1$ and Cdc42 becomes dominant at tip 2; see the red trajectory in Fig. 9(c,d). On the other

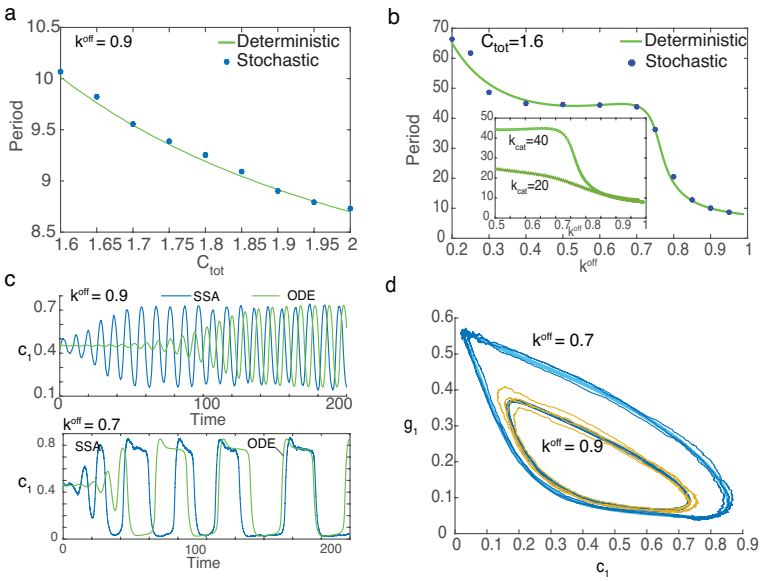

Figure 8: Comparison of deterministic and stochastic oscillations in the parameter regime where the deterministic system converges to an oscillation. (a) Period vs. C_{tot} with a fixed $k^{\text{off}} = 0.9$. As C_{tot} increases, the period of deterministic oscillation (green) and the period of stochastic oscillation (green) decrease. The averaged period of stochastic oscillation is computed using 1000 realizations. (b) Period vs. k^{off}. As k_{off} decreases, the period of oscillation increases and there is a fast change when k_{off} decreases from 0.9 to 0.7. Such a fast change can be reduced if the autocatalysis rate k_{cat} is reduced from 40 to 20; see the inset. (c) Time-course plots of oscillations with $k^{\text{off}} = 0.9, 0.7$. As k^{off} decreases, both deterministic and stochastic oscillations change from a sinusoidal wave to a relaxation oscillation. The concentration c_1 and g_1 are normalized by C_{tot} and G_{tot}, respectively. (d) Periodic orbits in the (c_1, g_1) plane. Other parameters are the same as in Fig. 2. The time scale of 1 unit corresponds to 15 sec.

hand, if we reduce the amount of Cdc42 at tip 2 (IC (33)), the system will converge to another steady state with $c_1 > c_2$; see the orange trajectory in Fig. 9(c,d). With the initial condition (31), stochastic simulations approach one of the steady states; see black curves. As the deterministic system is quite sensitive to ICs, inherent fluctuations in the stochastic system help the trajectory escape the basin of attraction of the limit cycle and approach the stable steady state (see also Fig. 5).

4 Discussion

Polarity establishment has often been modeled using deterministic equations that ignore the discrete nature of molecules, and concentrations of molecular species are treated as continuous variables. For example, the deterministic model of Das et al. [14], added noise to parameter values in a DDE model to represent random fluctuations in order to capture the observed variability in concentration of Cdc42 between the two tips of the cell. Here, our stochastic model using a continuous-time Markov jump process with fixed parameters naturally describes inherent (intrinsic) fluctuations in the underlying biochemical system. We use this stochastic model to test the effect that cell size has on fluctuations, while keeping concentration of Cdc42 and GEF constant, which would not be possible to do in a deterministic model. Due to the fast diffusion coefficient of cytosolic Cdc42, we assume the system is well-mixed and do not consider the effect of diffusion in our stochastic model. The effect of diffusion and growing cell size in a stochastic model for Cdc42 oscillation will be considered separately in a future publication.

We find that for the symmetric steady state, where the amount of Cdc42 at the two tips should be identical according to the deterministic model, the amount of fluctuations in the difference between the

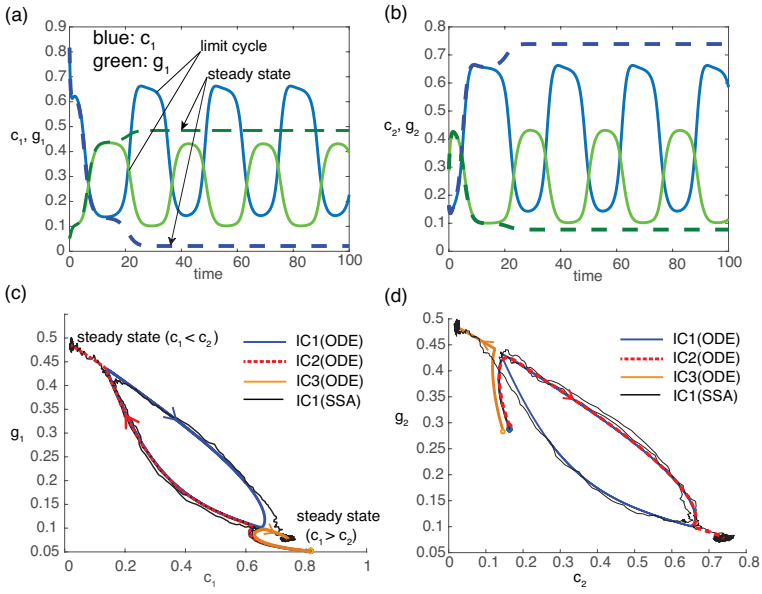

Figure 9: Near the infinite period bifurcation point $C_{\text{tot}} = 1.1$, the deterministic system converges to different attractors under small perturbations of initial conditions. (a,b) Time-course plots of Cdc42 and GEF at two tips. All the numerical solutions $c_{1,2}(g_{1,2})$ are rescaled by the total concentration $C_{\text{tot}}(G_{\text{tot}})$. The time scale of 1 unit corresponds to 15 sec(c,d) Trajectories in the (c_1, g_1) and (c_2, g_2) phase planes. Three initial conditions are used to generate different trajectories. IC1 (blue trajectory): $[c_1(0), c_2(0), g_1(0), g_2(0)] = [0.8980, 0.1809, 0.0770, 0.4300]$. IC2 (red trajectory): $[c_1(0), c_2(0), g_1(0), g_2(0)] = [0.8980, 0.1809, 0.0770, 0.44]$. IC3 (orange trajectory): $[c_1(0), c_2(0), g_1(0), g_2(0)] = [0.8980, 0.16, 0.0770, 0.43]$. Two stochastic trajectories using IC1 are shown in black. Other parameters are the same as in Fig. 5.

normalized species copy number and the concentration greatly exceeds $O(N^{-1/2})$, which one would naively expect in stochastic simulations. Instead, we observe high-amplitude stochastic oscillations around this deterministic steady state. For a dynamical system with a decaying oscillation, McKane et al. [51] have previously shown that stochastic kinetics of the dynamical system can give rise to a sustained oscillation with a larger amplitude. Such a phenomenon (termed coherence resonance) has also been observed in other biological models including a predator-prey model [52], a cyclic Lotka–Volterra model [58], and a stochastic Wilson–Cowan model [11]. We determine the dominant frequency of these quasi-cycles numerically, and analytically derive a formula for the power spectrum applying the method by McKane et al. [51]. We also showed that the power spectrum has a local maximum very close to the observed dominant frequency. A more rigorous treatment of coherence resonance using multi-scale analysis can be found in [46].

There is a wide literature on the effect of stochastic chemical kinetics on oscillations in cell biology. The Tyson group has compared deterministic and stochastic models of cell cycle regulation [38, 6]. Variability in oscillations of the p53-Mdm2 regulatory circuit is thought to be due to low-frequency noise in protein production rates [26]. The robustness of circadian oscillations depend on both the number of molecules and the degree of cooperativity of the negative feedback [28, 29, 20]. Spatiotemporal oscillations of the Min proteins from pole to pole have been observed in *E. coli*. Some stochastic models of Min oscillations include [2, 65, 55, 32, 40]. Similar to Howard and Rutenberg [32], we also find that in some parameter regimes, stochastic effects are necessary to observe oscillations in the model, and that cells can, in principle, use these fluctuations to generate pattern forming dynamics when molecule number is in the thousands. In an environment with changing external cues, such as nutrient or pheromone gradients, Cdc42 fluctuations may allow fission yeast to adapt and redirect the direction of growth. However, for very small cells (with r=0.5 μm), where molecule number is in the hundreds, fluctuations lead to random

switching from a stable limit cycle to a steady state and back, or extinguish oscillations altogether. Modeling studies in budding yeast estimate the number of Cdc42 molecules to be around 3000 molecules [42]. However, note that an estimate for total number of Cdc42 is about 80,000 molecules in fission yeast (Pombase `https://www.pombase.org/gene/SPAC110.03`). For GEF1 there is estimated 45,000 molecules per cell. However there are only about 10 RNA molecules of Cdc42 per cell and only 3 or so RNA molecules for GEF1.

We focus on a direct comparison between the deterministic and stochastic models. The propensity in our stochastic model is derived using a heuristic method. We replace the concentration variable in the deterministic rate by the normalized copy number n/Ω since our model for Cdc42 does not include a bimolecular (or higher-order) reaction between the same species. The chemical rate constants that appear in the deterministic equations represent macroscopic quantities that depend on stochastic chemical kinetics, which are mass action [27]. To re-formulate more complicated nonlinear association rates as mass action kinetics would require a replacement of the current non-linear terms in system (7) by specific enzyme kinetics. Such a description would involve the introduction of new variables and new assumptions, as well as relatively ad hoc choices regarding their reactions and behaviour, obfuscating the comparison between the deterministic and stochastic models. Stochastic simulation and linear noise approximation for the Hill-type reaction kinetics are still an active area of research [7, 62, 41, 48]. In [62], the authors simulate a specific model of gene regulatory network with a negative feedback using two algorithms. One algorithm is derived from a master equation that models a reduced reaction with a Hill-type rate. The other algorithm is derived from a master equation that models a set of elementary reactions with mass action kinetics. By comparing the coefficients of variance of the simulation results, the authors suggest that stochastic simulation by the Gillespie method underestimates the size of fluctuations for Hill-type kinetics. Whether this conclusion holds for a general reaction with other kinetics remains unknown.

In addition to the stochastic model using a continuous-time Markov jump process which is equivalent to the chemical master equation (CME), other approaches for modeling stochastic biochemical reactions include the chemical Langevin equation (CLE) and its associated chemical Fokker–Planck equation (CFPE). A thorough discussion of these methods can be found in a recent review [60]. The major limitation of the CME is that the analytical solution is often unknown and the numerical simulation is expensive. An alternative is to use the CLE, which is a diffusion approximation to the CME ([37]). To achieve a good approximation, the CLE requires the molecule number to be large. One known issue of the CLE is that numerical integrations of the CLE can result in negative numbers of molecules [49, 70]. This is likely to occur in our model since the mean concentration of Cdc42 at one end can be low and thus the molecules at this end are likely to be depleted in a stochastic model. To avoid the issue of producing negative numbers, some modification of the standard CLE would be necessary.

One remaining mathematical task is to analyze the dynamical behavior in the parameter regime where the deterministic system has an infinite period bifurcation point. Whether such an infinite-period bifurcation would occur in the stochastic model remains unknown. For a system with a saddle-node infinite period bifurcation, Erban et al. [18] showed that the period of stochastic oscillation remains finite for a finite system size. For our system, the difficulty in doing similar analysis lies in coexistence of oscillations and steady states. As shown in Fig. 7, with stochastic chemical kinetics, transitions between steady states and cycles are likely to occur. A potential extension is to calculate the mean residence time near a steady state or a cycle and the mean switching time between cycles and steady states. One related task is to estimate the basins of attraction of the deterministic model using the method proposed in [13] and to explore how stochastic fluctuations may affect the basins. Our result is based on numerical simulations, and rigorous studies of the dynamics of the stochastic system including the existence of stationary distributions and asymptotic stability of stochastic cycles remain open.

Acknowledgments

BX is supported by the Robert and Sara Lumpkins Endowment for Postdoctoral Fellows in Applied and Computational Math and Statistics at the University of Notre Dame. HWK is supported by NSF grant DMS-1620403. AJ is supported by NSF grant DMS-1615800. AJ and BX acknowledge the assistance of the Notre Dame Center for Research Computing (CRC).

Appendices

A Scaling of the Deterministic and Stochastic Models

A.1 Dimensionalization of Deterministic Model

Note that our deterministic model [73] used dimensionless units including all the concentrations and the cell size parameter L. Hence, for the stochastic simulation we need to reconstruct the dimensional model with parameters that have appropriate units. Recall that there are three types of variables with different units: length, time, and concentration. For concentrations, we have both membrane and cytosolic concentrations. One choice for these two concentrations are proteins per unit area (μm^{-2}) and protein copy numbers per unit volume (μm^{-3}).

Denote $\tilde{x}$ and $\tilde{t}$ by the length and time variables in dimensions. Denote $\tilde{C}(\tilde{G})$ and $\tilde{c}(\tilde{g})$ by the cytosolic and membrane concentrations of Cdc42(GEF) in dimensions. Consider the change of variables

$$\tilde{x} = \alpha x, \quad \tilde{t} = \beta t, \quad \tilde{C}(\tilde{x}, \tilde{t}) = \gamma C(x, t), \quad \tilde{c}_{1,2}(\tilde{t}) = \gamma_m c_{1,2}(t). \tag{34}$$

Here α represents the units of length. Since $L = 1$ corresponds to 9μm, we set $\alpha = 9\mu$m. Also, the Cdc42 dissociation rate $k^- = 1$ corresponds to $4\,\text{min}^{-1}$[14], hence we take $\beta = 1/4\,\text{min} = 15\,\text{sec}$. We will discuss the units of concentrations (i.e., values of γ, γ_m) at a later time.

Using equation (34), we have

$$\frac{\partial C}{\partial t} = \frac{\beta}{\gamma}\frac{\partial \tilde{C}}{\partial \tilde{t}}, \quad \frac{\partial C}{\partial x} = \frac{\alpha}{\gamma}\frac{\partial \tilde{C}}{\partial \tilde{x}}, \quad \frac{\partial^2 C}{\partial x^2} = \frac{\alpha^2}{\gamma}\frac{\partial^2 \tilde{C}}{\partial \tilde{x}^2}, \quad \frac{\mathrm{d}c_i}{\mathrm{d}t} = \frac{\beta}{\gamma_m}\frac{\mathrm{d}\tilde{c}_i}{\mathrm{d}\tilde{t}}. \tag{35}$$

Hence from (1), the diffusion equation and ODEs with dimensions are given by

$$\frac{\partial \tilde{C}}{\partial \tilde{t}}(\tilde{x}, \tilde{t}) = \frac{D_C \alpha^2}{\beta}\frac{\partial^2 \tilde{C}}{\partial \tilde{x}^2}, \tag{36a}$$

$$\frac{\mathrm{d}\tilde{c}_1}{\mathrm{d}\tilde{t}}(\tilde{t}) = \left(\frac{k_0}{\gamma\beta} + \frac{k_{cat}}{\gamma\gamma_m^2\beta}\tilde{c}_1^2\right)\tilde{g}_1\tilde{C}(0, \tilde{t}) - \frac{k^-}{\beta}\tilde{c}_1(\tilde{t}), \tag{36b}$$

$$\frac{\mathrm{d}\tilde{g}_1}{\mathrm{d}\tilde{t}}(\tilde{t}) = \frac{k^{\text{on}_{\max}}/\beta}{1 + \kappa\tilde{c}_1^2/\gamma_m^2}\frac{\gamma_m}{\gamma}\tilde{G}(0, \tilde{t}) - \frac{k^{\text{off}}}{\beta}\tilde{g}_1(\tilde{t}). \tag{36c}$$

We list the dimensions of rates below.

$$\tilde{k}_0 = \frac{k_0}{\gamma\beta}\frac{1}{[\text{conc.}] \times \text{sec}}, \quad \tilde{k}_{\text{cat}} = \frac{k_{cat}}{\gamma\gamma_m^2\beta}\frac{1}{[\text{conc.}]_{\text{m}}^2 \times [\text{conc.}] \times \text{sec}}, \tag{37a}$$

$$\tilde{k}^{\text{on}}_{\max} = \frac{k^{\text{on}}_{\max}}{\beta}\frac{\gamma_m}{\gamma}\frac{[\text{conc.}]_{\text{m}}}{[\text{conc.}] \times \text{sec}}, \quad \tilde{\kappa} = \frac{\kappa}{\gamma_m^2}\frac{1}{[\text{conc.}]_{\text{m}}^2}, \quad \tilde{k}^{\text{off}} = \frac{k^{\text{off}}}{\beta}\frac{1}{\text{sec}}. \tag{37b}$$

Here [conc.] represents cytosolic concentration and $[\text{conc.}]_{\text{m}}$ represents membrane concentration. It remains to determine the units of concentrations γ and γ_m and the corresponding order of magnitude.

A.2 Units of Concentration and Model Geometry

For the stochastic model geometry, we model the rod-shaped cell as a cylinder. In this case, each cell tip is a small disk with a radius r and a small thickness. This is the model geometry that is consistent with our one-dimensional deterministic model. For molecules attached to the cell membrane, we measure

the concentration using molecular copy number per cross-section area since the thickness is fixed. For cytosolic concentration, we use the units of molecular copy number per volume (μm^3).

Let $\gamma_m = \frac{\#}{\text{area}} = n_1 \mu\text{m}^{-2}$ and $\gamma = \frac{\#}{\text{volume}} = n_c \mu\text{m}^{-3}$. Here n_1 and n_c are numbers that represent the order of magnitude. The number of molecules in each compartment is given by

$$n_1 = \tilde{c}_1 A, \quad m_1 = \tilde{g}_1 A, \quad n_c(\tilde{t}) = \tilde{C}(\tilde{t})V, \quad m_c(\tilde{t}) = \tilde{G}(\tilde{t})V. \tag{38}$$

Note that in the last two equations, we drop the spatial-dependence. This holds when diffusion in the cytosol is fast. The conservation equation is then given by

$$\begin{aligned} N_{\text{cdc}} = n_1 + n_2 + n_c \Rightarrow \tilde{c}_1 A + \tilde{c}_2 A + \tilde{C}(\tilde{t})V = \tilde{C}_{\text{tot}} V, \\ \Rightarrow \tilde{C}(\tilde{t}) = \frac{\tilde{C}_{\text{tot}} V/A - \tilde{c}_1 - \tilde{c}_2}{V/A}. \end{aligned} \tag{39}$$

Since we model the cell as a cylinder, the ratio V/A is given by

$$V \approx A \times (\alpha L), \tag{40}$$

where $\alpha = 9\mu$m. Equation (39) becomes

$$\tilde{C}(\tilde{t}) = \frac{\tilde{C}_{\text{tot}} \alpha L - \tilde{c}_1 - \tilde{c}_2}{\alpha L}. \tag{41}$$

We now rewrite the above equation in terms of the dimensionless variables. Using the change of variables (34) to remove the tilde notations gives

$$\begin{aligned} C(t)\gamma = \frac{C_{tot}\gamma\alpha L - c_1\gamma_m - c_2\gamma_m}{\alpha L}, \\ \Rightarrow C(t)\frac{\alpha\gamma}{\gamma_m} = \frac{C_{tot} L(\alpha\gamma/\gamma_m) - c_1 - c_2}{L}. \end{aligned} \tag{42}$$

Suppose we choose γ and γ_m such that

$$\frac{\alpha\gamma}{\gamma_m} = 1. \tag{43}$$

Then we can recover the conservation equation (6).

A.3 Derivation of Stochastic Rates

We now write down the equation for the number of molecules in each compartment using equation (38) and the differential equations (36). The ODEs for the number of Cdc42 at tip1 (n_1) and the number of GEF at tip1 (m_1) are given by

$$\frac{\mathrm{d}n_1}{\mathrm{d}\tilde{t}}(\tilde{t}) = \left(\frac{k_0}{\gamma\beta} + \frac{k_{cat}}{\gamma\gamma_m^2\beta}\frac{n_1^2}{A^2}\right) m_1 \frac{n_c(\tilde{t})}{V} - \frac{k^-}{\beta} n_1(\tilde{t}), \tag{44a}$$

$$\frac{\mathrm{d}m_1}{\mathrm{d}\tilde{t}}(\tilde{t}) = \frac{k^{\text{on}}_{\text{max}}/\beta}{1 + \kappa n_1^2/(\gamma_m^2 A^2)} \frac{\gamma_m}{\gamma}\frac{A}{V} m_c(\tilde{t}) - \frac{k^{\text{off}}}{\beta} m_1(\tilde{t}). \tag{44b}$$

Our goal is to derive the stochastic rates. The above ODEs imply the rescaling relations

$$k_0' = \frac{\tilde{k}_0}{V} = \frac{k_0}{\gamma\beta V}, \tag{45a}$$

$$k_{\text{cat}}' = \frac{\tilde{k}_{cat}}{A^2 V} = \frac{k_{cat}}{\gamma\gamma_m^2\beta}\frac{1}{A^2 V}, \tag{45b}$$

$$k_{\text{on}}' = \frac{\tilde{k}^{\text{on}} A}{V} = \frac{k_{\text{max}}^{\text{on}}\gamma_m}{\gamma\beta}\frac{A}{V}, \tag{45c}$$

$$\kappa' = \frac{\tilde{\kappa}}{A^2} = \frac{\kappa}{\gamma_m^2 A^2}, \tag{45d}$$

$$k_-' = \tilde{k}_- = \frac{k_-}{\beta}, \quad k_{\text{off}}' = \tilde{k}_{\text{off}} = \frac{k^{\text{off}}}{\beta}. \tag{45e}$$

Here the rates with the $'$ notation represent the rates we use in stochastic simulation, the rates with the tilde notation represent the rates in physical units, and the rates without any notation are dimensionless.

Using the relations $V = A\alpha L$ and $\alpha\gamma = \gamma_m$, we simplify the rescaling relation as

$$k_0' = \frac{k_0}{\gamma\beta\alpha L A} = \frac{k_0}{\gamma_m\beta L A}, \tag{46a}$$

$$k_{\text{cat}}' = \frac{k_{cat}}{\gamma_m^3 A^3 L\beta}, \tag{46b}$$

$$k_{\text{on}}' = \frac{k_{\text{max}}^{\text{on}}\gamma_m}{\gamma\beta}\frac{A}{V} = \frac{k_{\text{max}}^{\text{on}}}{\beta L}, \tag{46c}$$

$$\kappa' = \frac{\kappa}{\gamma_m^2 A^2}, \tag{46d}$$

$$k_-' = \frac{k_-}{\beta}, \quad k_{\text{off}}' = \frac{k^{\text{off}}}{\beta}. \tag{46e}$$

Setting $\gamma_m = 602$, we recover equation (10). Note that the unit of all stochastic rate constants except for κ' is per $1/4\,\text{min}$ ($15\,\text{sec}$) due to the factor $1/\beta$ in (46).

A.4 Derivation of the Reduced ODE Model from the Stochastic Model

Remind that the numbers of molecules of Cdc42 at tip1, at tip2, and in the cytosol at time $\tilde{t}$ by $n_1(\tilde{t})$, $n_2(\tilde{t})$, and $n_c(\tilde{t})$. Similarly, the numbers of molecules of GEF at tip1, tip2, and in the cytosol at time $\tilde{t}$ are $m_1(\tilde{t})$, $m_2(\tilde{t})$, and $m_c(\tilde{t})$. Then, the species copy numbers are governed by the following stochastic equations

$$\begin{aligned}
n_i(\tilde{t}) &= n_i(0) + Y_{i,1}\left(\int_0^{\tilde{t}} \left(k_0' + k_{\text{cat}}' n_i(\tilde{s})^2\right) m_i(\tilde{s}) n_c(\tilde{s})\, d\tilde{s}\right) - Y_{i,2}\left(\int_0^{\tilde{t}} k_-' n_i(\tilde{s})\, d\tilde{s}\right), \quad i = 1, 2,\\
n_c(\tilde{t}) &= n_c(0) + \sum_{i=1}^{2}\left[-Y_{i,1}\left(\int_0^{\tilde{t}} \left(k_0' + k_{\text{cat}}' n_i(\tilde{s})^2\right) m_i(\tilde{s}) n_c(\tilde{s})\, d\tilde{s}\right) + Y_{i,2}\left(\int_0^{\tilde{t}} k_-' n_i(\tilde{s})\, d\tilde{s}\right)\right],\\
m_i(\tilde{t}) &= m_i(0) + Y_{i,3}\left(\int_0^{\tilde{t}} \frac{k_{\text{on}}'}{1+\kappa' n_i(\tilde{s})^2} m_c(\tilde{s})\, d\tilde{s}\right) - Y_{i,4}\left(\int_0^{\tilde{t}} k_{\text{off}}' m_i(\tilde{s})\, d\tilde{s}\right), \quad i = 1, 2,\\
m_c(\tilde{t}) &= m_c(0) + \sum_{i=1}^{2}\left[-Y_{i,3}\left(\int_0^{\tilde{t}} \frac{k_{\text{on}}'}{1+\kappa' n_i(\tilde{s})^2} m_c(\tilde{s})\, d\tilde{s}\right) + Y_{i,4}\left(\int_0^{\tilde{t}} k_{\text{off}}' m_i(\tilde{s})\, d\tilde{s}\right)\right],
\end{aligned} \tag{47}$$

where Y_k's are independent Poisson processes. Adding the equations for CDC42 (or GEF) in (47), the total number of molecules of Cdc42 (or GEF) is conserved as

$$\begin{aligned} n_1(\tilde{t}) + n_2(\tilde{t}) + n_c(\tilde{t}) &= n_1(0) + n_2(0) + n_c(0) \equiv N_{cdc}, \\ m_1(\tilde{t}) + m_2(\tilde{t}) + m_c(\tilde{t}) &= m_1(0) + m_2(0) + m_c(0) \equiv N_{gef}. \end{aligned} \tag{48}$$

Plugging in $\tilde{t} = \beta t$ and using the change of variables ($\tilde{s} = \beta s$), (47) become

$$\begin{aligned} n_i(\beta t) &= n_i(0) + Y_{i,1}\left(\int_0^t \left(k_0' + k_{\text{cat}}' n_i(\beta s)^2\right) m_i(\beta s) n_c(\beta s)\beta\, ds\right) - Y_{i,2}\left(\int_0^t k_-' n_i(\beta s)\beta\, ds\right), \\ n_c(\beta t) &= n_c(0) + \sum_{i=1}^{2}\left[-Y_{i,1}\left(\int_0^t \left(k_0' + k_{\text{cat}}' n_i(\beta s)^2\right) m_i(\beta s) n_c(\beta s)\beta\, ds\right) + Y_{i,2}\left(\int_0^t k_-' n_i(\beta s)\beta\, ds\right)\right], \\ m_i(\beta t) &= m_i(0) + Y_{i,3}\left(\int_0^t \frac{k_{\text{on}}'}{1+\kappa' n_i(\beta s)^2} m_c(\beta s)\beta\, ds\right) - Y_{i,4}\left(\int_0^t k_{\text{off}}' m_i(\beta s)\beta\, ds\right), \\ m_c(\beta t) &= m_c(0) + \sum_{i=1}^{2}\left[-Y_{i,3}\left(\int_0^t \frac{k_{\text{on}}'}{1+\kappa' n_i(\beta s)^2} m_c(\beta s)\beta\, ds\right) + Y_{i,4}\left(\int_0^t k_{\text{off}}' m_i(\beta s)\beta\, ds\right)\right], \end{aligned} \tag{49}$$

for $i = 1, 2$. Assuming all species copy numbers are of the same order, we normalize the species copy numbers by a scaling parameter $N = \gamma_m A = 602A$. Define normalized variables as

$$c_i^N(t) = \frac{n_i(\beta t)}{N}, \qquad C^N(t) = \frac{n_c(\beta t)}{NL}, \qquad g_i^N(t) = \frac{m_i(\beta t)}{N}, \qquad G^N(t) = \frac{m_c(\beta t)}{NL}, \tag{50}$$

for $i = 1, 2$.

We express the stochastic rate constants in (46) using N as the following:

$$k_0' = \frac{k_0}{N\beta L}, \quad k_{\text{cat}}' = \frac{k_{cat}}{N^3\beta L}, \quad k_{\text{on}}' = \frac{k_{\text{max}}^{\text{on}}}{\beta L}, \quad \kappa' = \frac{\kappa}{N^2}, \quad k_-' = \frac{k_-}{\beta}, \quad k_{\text{off}}' = \frac{k^{\text{off}}}{\beta}. \tag{51}$$

Then, plugging in the normalized variables and scaled rate constants in (50) and (51), (49) becomes

$$\begin{aligned} c_i^N(t) &= c_i^N(0) + \frac{1}{N} Y_{i,1}\left(\int_0^t N\left(k_0 + k_{cat} c_i^N(s)^2\right) g_i^N(s) C^N(s)\, ds\right) - \frac{1}{N} Y_{i,2}\left(\int_0^t N k_- c_i^N(s)\, ds\right), \\ C^N(t) &= C^N(0) + \sum_{i=1}^{2} \frac{1}{NL}\left[-Y_{i,1}\left(\int_0^t N\left(k_0 + k_{cat} c_i^N(s)^2\right) g_i^N(s) C^N(s)\, ds\right) + Y_{i,2}\left(\int_0^t N k_- c_i^N(s)\, ds\right)\right], \\ g_i^N(t) &= g_i^N(0) + \frac{1}{N} Y_{i,3}\left(\int_0^t \frac{N k_{\text{max}}^{\text{on}}}{1+\kappa c_i^N(s)^2} G^N(s)\, ds\right) - \frac{1}{N} Y_{i,4}\left(\int_0^t N k^{\text{off}} g_i^N(s)\, ds\right), \\ G^N(t) &= G^N(0) + \sum_{i=1}^{2} \frac{1}{NL}\left[-Y_{i,3}\left(\int_0^t \frac{N k_{\text{max}}^{\text{on}}}{1+\kappa c_i^N(s)^2} G^N(s)\, ds\right) + Y_{i,4}\left(\int_0^t N k^{\text{off}} g_i^N(s)\, ds\right)\right], \end{aligned} \tag{52}$$

for $i = 1, 2$. The strong law of large numbers states that, for a unit Poisson process Y, $\frac{1}{N} Y(Nu) \to u$ almost surely as $N \to \infty$. Therefore, assuming that $c_i^N(0) \to c_i(0)$, $C^N(0) \to C(0)$, $g_i^N(0) \to g_i(0)$, and

$G^N(0) \to G(0)$ as $N \to \infty$, $X^N \equiv \left(c_1^N, c_2^N, C^N, g_1^N, g_2^N, G^N\right)$ converges to the limit which is a solution of

$$\begin{aligned}
c_i(t) &= c_i(0) + \int_0^t \left[\left(k_0 + k_{cat} c_i(s)^2\right) g_i(s) C(s) - k_- c_i(s)\right] ds, \\
C(t) &= C(0) + \frac{1}{L} \int_0^t \sum_{i=1}^{2} \left[-\left(k_0 + k_{cat} c_i(s)^2\right) g_i(s) C(s) + k_- c_i(s)\right] ds, \\
g_i(t) &= g_i(0) + \int_0^t \left[\frac{k_{\max}^{\text{on}}}{1 + \kappa c_i(s)^2} G(s) - k^{\text{off}} g_i(s)\right] ds, \\
G(t) &= G(0) + \frac{1}{L} \int_0^t \sum_{i=1}^{2} \left[-\frac{k_{\max}^{\text{on}}}{1 + \kappa c_i(s)^2} G(s) + k^{\text{off}} g_i(s)\right] ds,
\end{aligned} \tag{53}$$

for $i = 1, 2$ as $N \to \infty$. Note that c_i and g_i are the solution of the reduced ODE model for Cdc42 and GEF given in (7) and the total concentrations of Cdc42 and GEF are conserved as

$$\begin{aligned}
\frac{c_1(t) + c_2(t)}{L} + C(t) &\equiv C_{tot}, \\
\frac{g_1(t) + g_2(t)}{L} + G(t) &\equiv G_{tot},
\end{aligned} \tag{54}$$

which is consistent to (6). Setting $N = 602A$ and $t = 0$ in (50), we obtain that

$$n_i(0) = 602A\, c_i(0), \quad n_c(0) = 602AL\, C(0), \quad m_i(0) = 602A\, g_i(0), \quad m_c(0) = 602AL\, G(0), \tag{55}$$

for $i = 1, 2$. Then, (55), (48), and (54) provides how C_{tot} and N_{cdc} (G_{tot} and N_{gef}) are related as follow:

$$\begin{aligned}
N_{cdc} &= 602A(c_1(t) + c_2(t) + LC(t)) = 602AL\, C_{tot}, \\
N_{gef} &= 602A(g_1(t) + g_2(t) + LG(t)) = 602AL\, G_{tot}.
\end{aligned} \tag{56}$$

B Power Spectrum Analysis

B.1 Discrete Fourier transform

Here we use the fast Fourier transform to estimate the temporal power spectrum density of a discrete time series $\{n_1(t_i)\}_{i=1}^{N_t}$ generated by Gillespie's algorithm. We first replace $n_1(t_i)$ by $n_1(t_i) - n_1^*$. The default time interval is given by $t = 0 : \Delta t : t_{\text{end}}$ with $t_{\text{end}} = 200$ and a uniform time step $\Delta t = 0.001$. For the frequency interval, we set the sample frequency $f_s = 1/\Delta t = 1000$ and define the frequency domain by

$$ff = [0 : N_t - 1] * \Delta f, \quad \Delta f = \frac{f_s}{N_t}. \tag{57}$$

Here N_t is the length of the time series. For each frequency f_k, the discrete Fourier transform of $n_1(t)$ is given by

$$\tilde{n}_1(k) := \sum_{j=0}^{N_t - 1} n_1(t_j) \mathrm{e}^{-2\pi i j k / N}. \tag{58}$$

Define the one-sided power spectrum $P(k)$ by [57, 64]

$$P(k) = \begin{cases} \dfrac{|\tilde{n}_1(k)|^2}{N_t^2}, & k = 0,\, N_t/2, \\ \dfrac{|\tilde{n}_1(k)|^2 + |\tilde{n}_1(N_t - k)|^2}{N_t^2}, & 1 \le k \le N_t/2 - 1. \end{cases} \tag{59}$$

The power spectral density (PSD) over the frequency range $(f_k - f_s/(2N_t), f_k + f_s/(2N_t))$ is given by

$$S(f_k \pm \frac{1}{2} f_s) = \frac{P(k)}{\Delta f} = \frac{|\tilde{n}_1(k)|^2 + |\tilde{n}_1(N_t - k)|^2}{N_t f_s}. \tag{60}$$

The corresponding PSD over the angular frequency range $(\omega_k - \Delta\omega/2, \omega_k + \Delta\omega/2)$ is

$$S(\omega_k \pm \frac{1}{2}\Delta\omega) = \frac{P(k)}{\Delta\omega}. \tag{61}$$

Here the angular frequency increment is$\Delta\omega = 2\pi f_s/N_t$. Finally, we average the PSD of a single realization r over R realizations to obtain a numerical approximation for the PSD. Denote the PSD of a single realization r by $S^r(\omega_k)$. The averaged PSD is given by

$$S(\omega_k) = \frac{1}{R}\sum_{r=1}^{R} S^r(\omega_k). \tag{62}$$

B.2 MATLAB code

```
%read data
x=n_1/N;% N is the system size
idx1=ceil(length(x)*0.5);
x=x(idx1:end);
t=time(idx1:end);
dt=t(2)-t(1);
%remove the steady state component (x_ss is close to mean(xd))
xd=x-x_ss;

% Zero-padding: add zeros to x so that length(x) equals to a power of 2.
Nt = 2^nextpow2(length(xd));
% sample frequency
fs = 1/dt;
ff = [0:Nt-1]*fs/Nt;% frequency vector
df=ff(2)-ff(1);
%FFT
q = fft(xd,Nt);
%power spectrum
Pxx = q.*conj(q)/Nt^2;
%power spectrum density(psd)
Sxx=Pxx/df;
% one-sided psd
ff=ff(1:floor(Nt/2)+1);
Sxx=Sxx(1:floor(Nt/2)+1);
Sxx(2:end-1)=2*Sxx(2:end-1);
% psd in angular frequency
w=2*pi*ff;
Sw=Pxx/(df*2*pi);

% find the dominant frequency f
[pwrest,idx] = max(Sxx);
fprintf('The maximum power(using FFT) occurs at f = %3.3f \n',ff(idx))
```

References

1. Steven J Altschuler, Sigurd B Angenent, Yanqin Wang, and Lani F Wu. On the spontaneous emergence of cell polarity. *Nature*, 454(7206):886–889, 2008.

2. Artemij Amiranashvili, Nikolas D Schnellbächer, and Ulrich S Schwarz. Stochastic switching between multistable oscillation patterns of the Min-system. *New Journal of Physics*, 18(9):093049, 2016.

3. David F Anderson, Daniele Cappelletti, and Thomas G Kurtz. Finite time distributions of stochastically modeled chemical systems with absolute concentration robustness. *SIAM Journal on Applied Dynamical Systems*, 16(3):1309–1339, 2017.

4. David F Anderson, Germán A Enciso, and Matthew D Johnston. Stochastic analysis of biochemical reaction networks with absolute concentration robustness. *Journal of The Royal Society Interface*, 11(93):20130943, 2014.

5. Max Ashkenazi and HG Othmer. Spatial patterns in coupled biochemical oscillators. *Journal of Mathematical Biology*, 5(4):305–350, 1978.

6. Debashis Barik, David A Ball, Jean Peccoud, and John J Tyson. A stochastic model of the yeast cell cycle reveals roles for feedback regulation in limiting cellular variability. *PLoS computational biology*, 12(12):e1005230, 2016.

7. Debashis Barik, Mark R Paul, William T Baumann, Yang Cao, and John J Tyson. Stochastic simulation of enzyme-catalyzed reactions with disparate timescales. *Biophysical journal*, 95(8):3563–3574, 2008.

8. Felipe O Bendezú, Vincent Vincenzetti, Dimitrios Vavylonis, Romain Wyss, Horst Vogel, and Sophie G Martin. Spontaneous Cdc42 polarization independent of GDI-mediated extraction and actin-based trafficking. *PLoS biology*, 13(4):e1002097, 2015.

9. Roberto Benzi, Alfonso Sutera, and Angelo Vulpiani. The mechanism of stochastic resonance. *Journal of Physics A: mathematical and general*, 14(11):L453, 1981.

10. Daria Bonazzi, Armin Haupt, Hirokazu Tanimoto, Delphine Delacour, Delphine Salort, and Nicolas Minc. Actin-based transport adapts polarity domain size to local cellular curvature. *Current Biology*, 25(20):2677–2683, 2015.

11. Paul C Bressloff. Metastable states and quasicycles in a stochastic Wilson-Cowan model of neuronal population dynamics. *Physical Review E*, 82(5):051903, 2010.

12. Fred Chang and Sophie G Martin. Shaping fission yeast with microtubules. *Cold Spring Harbor perspectives in biology*, 1(1):a001347, 2009.

13. H-D Chiang and James S Thorp. Stability regions of nonlinear dynamical systems: A constructive methodology. *IEEE Transactions on Automatic Control*, 34(12):1229–1241, 1989.

14. Maitreyi Das, Tyler Drake, David J Wiley, Peter Buchwald, Dimitrios Vavylonis, and Fulvia Verde. Oscillatory dynamics of Cdc42 GTPase in the control of polarized growth. *Science*, 337(6091):239–243, 2012.

15. Thierry Dauxois, Francesca Di Patti, Duccio Fanelli, and Alan J McKane. Enhanced stochastic oscillations in autocatalytic reactions. *Physical Review E*, 79(3):036112, 2009.

16. German A Enciso. Transient absolute robustness in stochastic biochemical networks. *Journal of The Royal Society Interface*, 13(121):20160475, 2016.

17. Makoto Endo, Mikako Shirouzu, and Shigeyuki Yokoyama. The Cdc42 binding and scaffolding activities of the fission yeast adaptor protein scd2. *Journal of Biological Chemistry*, 278(2):843–852, 2003.

18. Radek Erban, S Jonathan Chapman, Ioannis G Kevrekidis, and Tomáš Vejchodskỳ. Analysis of a stochastic chemical system close to a SNIPER bifurcation of its mean-field model. *SIAM Journal on Applied Mathematics*, 70(3):984–1016, 2009.

19. Sandrine Etienne-Manneville and Alan Hall. Rho GTPases in cell biology. *Nature*, 420(6916):629, 2002.

20. Daniel B Forger and Charles S Peskin. Stochastic simulation of the mammalian circadian clock. *Proceedings of the National Academy of Sciences*, 102(2):321–324, 2005.

21. Tina Freisinger, Ben Klünder, Jared Johnson, Nikola Müller, Garwin Pichler, Gisela Beck, Michael Costanzo, Charles Boone, Richard A Cerione, Erwin Frey, and Roland Wedlich-Söldner. Establishment of a robust single axis of cell polarity by coupling multiple positive feedback loops. *Nature communications*, 4:1807, 2013.

22. Luca Gammaitoni, Peter Hänggi, Peter Jung, and Fabio Marchesoni. Stochastic resonance. *Reviews of modern physics*, 70(1):223, 1998.

23. Hu Gang, T Ditzinger, CZ Ning, and H Haken. Stochastic resonance without external periodic force. *Physical Review Letters*, 71(6):807, 1993.

24. Crispin Gardiner. *Stochastic methods*, volume 4. springer Berlin, 2009.

25. Paul M Geffert. *Stochastic Non-Excitable Systems with Time Delay: Modulation of Noise Effects by Time-Delayed Feedback*. Springer, 2015.

26. Naama Geva-Zatorsky, Nitzan Rosenfeld, Shalev Itzkovitz, Ron Milo, Alex Sigal, Erez Dekel, Talia Yarnitzky, Yuvalal Liron, Paz Polak, Galit Lahav, and Uri Alon. Oscillations and variability in the p53 system. *Molecular systems biology*, 2:2006.0033, 2006.

27. Daniel Gillespie. Stochastic simulation of chemical kinetics. *Annual Review of Physical Chemistry*, 58:35–55, 2007.

28. Didier Gonze, José Halloy, and Albert Goldbeter. Deterministic versus stochastic models for circadian rhythms. *Journal of biological physics*, 28(4):637–653, 2002.

29. Didier Gonze, José Halloy, and Albert Goldbeter. Robustness of circadian rhythms with respect to molecular noise. *Proceedings of the National Academy of Sciences*, 99(2):673–678, 2002.

30. Andrew B Goryachev and Marcin Leda. Many roads to symmetry breaking: molecular mechanisms and theoretical models of yeast cell polarity. *Molecular biology of the cell*, 28(3):370–380, 2017.

31. Björn Hegemann, Michael Unger, Sung Sik Lee, Ingrid Stoffel-Studer, Jasmin van den Heuvel, Serge Pelet, Heinz Koeppl, and Matthias Peter. A cellular system for spatial signal decoding in chemical gradients. *Developmental cell*, 35(4):458–470, 2015.

32. Martin Howard and Andrew D Rutenberg. Pattern formation inside bacteria: fluctuations due to the low copy number of proteins. *Physical Review Letters*, 90(12):128102, 2003.

33. Jifeng Hu, Hye-Won Kang, and Hans G Othmer. Stochastic analysis of reaction–diffusion processes. *Bulletin of mathematical biology*, 76(4):854–894, 2014.

34. Alexandra Jilkine, Sigurd B Angenent, Lani F Wu, and Steven J Altschuler. A density-dependent switch drives stochastic clustering and polarization of signaling molecules. *PLoS computational biology*, 7(11):e1002271, 2011.

35. Jayme M Johnson, Meng Jin, and Daniel J Lew. Symmetry breaking and the establishment of cell polarity in budding yeast. *Current opinion in genetics & development*, 21(6):740–746, 2011.

36. Matthew D Johnston, David F Anderson, Gheorghe Craciun, and Robert Brijder. Conditions for extinction events in chemical reaction networks with discrete state spaces. *Journal of mathematical biology*, 76(6):1535–1558, 2018.

37. Hye-Won Kang, Thomas G Kurtz, and Lea Popovic. Central limit theorems and diffusion approximations for multiscale markov chain models. *The Annals of Applied Probability*, 24(2):721–759, 2014.

38. Sandip Kar, William T Baumann, Mark R Paul, and John J Tyson. Exploring the roles of noise in the eukaryotic cell cycle. *Proceedings of the National Academy of Sciences*, 106(16):6471–6476, 2009.

39. Joel Keizer. *Statistical Thermodynamics of Nonequilibrium Processes*. Springer Science & Business Media, 1987.

40. Rex A Kerr, Herbert Levine, Terrence J Sejnowski, and Wouter-Jan Rappel. Division accuracy in a stochastic model of Min oscillations in Escherichia coli. *Proceedings of the National Academy of Sciences of the United States of America*, 103(2):347–352, 2006.

41. Jae Kyoung Kim, Krešimir Josić, and Matthew R Bennett. The validity of quasi-steady-state approximations in discrete stochastic simulations. *Biophysical journal*, 107(3):783–793, 2014.

42. Ben Klünder, Tina Freisinger, Roland Wedlich-Söldner, and Erwin Frey. GDI-mediated cell polarization in yeast provides precise spatial and temporal control of Cdc42 signaling. *PLoS computational biology*, 9(12):e1003396, 2013.

43. Chun-Chen Kuo, Natasha S Savage, Hsin Chen, Chi-Fang Wu, Trevin R Zyla, and Daniel J Lew. Inhibitory GEF phosphorylation provides negative feedback in the yeast polarity circuit. *Current Biology*, 24(7):753–759, 2014.

44. TG Kurtz. Limit theorems for sequences of jump markov processes. *Journal of Applied Probability*, 8(2):344–356, 1971.

45. Thomas G Kurtz. The relationship between stochastic and deterministic models for chemical reactions. *The Journal of Chemical Physics*, 57(7):2976–2978, 1972.

46. Rachel Kuske, Luis F Gordillo, and Priscilla Greenwood. Sustained oscillations via coherence resonance in SIR. *Journal of theoretical biology*, 245(3):459–469, 2007.

47. Michael J Lawson, Brian Drawert, Mustafa Khammash, Linda Petzold, and Tau-Mu Yi. Spatial stochastic dynamics enable robust cell polarization. *PLoS computational biology*, 9(7):e1003139, 2013.

48. Ovidiu Lipan and Cameron Ferwerda. Hill functions for stochastic gene regulatory networks from master equations with split nodes and time-scale separation. *Physical Review E*, 97(2):022413, 2018.

49. Tiina Manninen, Marja-Leena Linne, and Keijo Ruohonen. Developing Itô stochastic differential equation models for neuronal signal transduction pathways. *Computational Biology and Chemistry*, 30(4):280–291, 2006.

50. Alan J McKane, Tommaso Biancalani, and Tim Rogers. Stochastic pattern formation and spontaneous polarisation: the linear noise approximation and beyond. *Bulletin of mathematical biology*, 76(4):895–921, 2014.

51. Alan J McKane, James D Nagy, Timothy J Newman, and Marianne O Stefanini. Amplified biochemical oscillations in cellular systems. *Journal of Statistical Physics*, 128(1-2):165–191, 2007.

52. Alan J McKane and Timothy J Newman. Predator-prey cycles from resonant amplification of demographic stochasticity. *Physical review letters*, 94(21):218102, 2005.

53. Hans G Othmer and John A Aldridge. The effects of cell density and metabolite flux on cellular dynamics. *Journal of mathematical biology*, 5(2):169–200, 1978.

54. Michael Pablo, Samuel A Ramirez, and Timothy C Elston. Particle-based simulations of polarity establishment reveal stochastic promotion of Turing pattern formation. *PLoS computational biology*, 14(3):e1006016, 2018.

55. Nenad Pavin, Hana Čipčić Paljetak, and Vladimir Krstić. Min-protein oscillations in escherichia coli with spontaneous formation of two-stranded filaments in a three-dimensional stochastic reaction-diffusion model. *Physical Review E*, 73(2):021904, 2006.

56. Arkady S Pikovsky and Jürgen Kurths. Coherence resonance in a noise-driven excitable system. *Physical Review Letters*, 78(5):775, 1997.

57. William H Press, Saul A Teukolsky, William T Vetterling, and Brian P Flannery. *Numerical recipes in C*, volume 2. Cambridge university press Cambridge, 1996.

58. Tobias Reichenbach, Mauro Mobilia, and Erwin Frey. Coexistence versus extinction in the stochastic cyclic Lotka-Volterra model. *Physical Review E*, 74(5):051907, 2006.

59. Michael Samoilov, Sergey Plyasunov, and Adam P Arkin. Stochastic amplification and signaling in enzymatic futile cycles through noise-induced bistability with oscillations. *Proceedings of the National Academy of Sciences of the United States of America*, 102(7):2310–2315, 2005.

60. David Schnoerr, Guido Sanguinetti, and Ramon Grima. Approximation and inference methods for stochastic biochemical kinetics—a tutorial review. *Journal of Physics A: Mathematical and Theoretical*, 50(9):093001, 2017.

61. Brian D Slaughter, Sarah E Smith, and Rong Li. Symmetry breaking in the life cycle of the budding yeast. *Cold Spring Harbor perspectives in biology*, 1(3):a003384, 2009.

62. Philipp Thomas, Arthur V Straube, and Ramon Grima. The slow-scale linear noise approximation: an accurate, reduced stochastic description of biochemical networks under timescale separation conditions. *BMC systems biology*, 6(1):39, 2012.

63. Philipp Thomas, Arthur V Straube, Jens Timmer, Christian Fleck, and Ramon Grima. Signatures of nonlinearity in single cell noise-induced oscillations. *Journal of theoretical biology*, 335:222–234, 2013.

64. David LK Toner and Ramon Grima. Molecular noise induces concentration oscillations in chemical systems with stable node steady states. *The Journal of chemical physics*, 138(5):02B602, 2013.

65. Filipe Tostevin and Martin Howard. A stochastic model of Min oscillations in Escherichia coli and Min protein segregation during cell division. *Physical biology*, 3(1):1, 2005.

66. OV Ushakov, H-J Wünsche, F Henneberger, IA Khovanov, Lutz Schimansky-Geier, and MA Zaks. Coherence resonance near a Hopf bifurcation. *Physical review letters*, 95(12):123903, 2005.

67. Nicolaas Godfried Van Kampen. *Stochastic processes in physics and chemistry*, volume 1. Elsevier, 1992.

68. Melissa Vellela and Hong Qian. A quasistationary analysis of a stochastic chemical reaction: Keizer's paradox. *Bulletin of mathematical biology*, 69(5):1727–1746, 2007.

69. Edward Wheatley and Katrin Rittinger. Interactions between Cdc42 and the scaffold protein Scd2: requirement of sh3 domains for gtpase binding. *Biochemical Journal*, 388(1):177–184, 2005.

70. Joshua Wilkie and Yin Mei Wong. Positivity preserving chemical langevin equations. *Chemical Physics*, 353(1-3):132–138, 2008.

71. Chi-Fang Wu and Daniel J Lew. Beyond symmetry-breaking: competition and negative feedback in GTPase regulation. *Trends in cell biology*, 23(10):476–483, 2013.

72. Bin Xu and Paul C Bressloff. A PDE-DDE model for cell polarization in fission yeast. *SIAM Journal on Applied Mathematics*, 76(5):1844–1870, 2016.

73. Bin Xu and Alexandra Jilkine. Modeling Cdc42 oscillation in fission yeast. *Biophysical Journal*, 114(3):711–722, 2018.

74. Anna Zakharova, Alexey Feoktistov, Tatyana Vadivasova, and Eckehard Schöll. Coherence resonance and stochastic synchronization in a nonlinear circuit near a subcritical Hopf bifurcation. *The European Physical Journal Special Topics*, 222(10):2481–2495, 2013.

75. Anna Zakharova, Tatjana Vadivasova, Vadim Anishchenko, Aneta Koseska, and Juergen Kurths. Stochastic bifurcations and coherencelike resonance in a self-sustained bistable noisy oscillator. *Physical Review E*, 81(1):011106, 2010.